DESIGN AND FABRICATION OF HIGHLY EFFICIENT ELECTROOPTIC MODULATORS USING BRAGG GRATING REFLECTORS

A Dissertation

by

RYOUNG-HAN KIM

Submitted to the Office of Graduate Studies of
Texas A&M University
in partial fulfillment of the requirements for the degree of

DOCTOR OF PHILOSOPHY

December 2005

Major Subject: Electrical Engineering

DESIGN AND FABRICATION OF HIGHLY EFFICIENT ELECTROOPTIC MODULATORS USING BRAGG GRATING REFLECTORS

A Dissertation

by

RYOUNG-HAN KIM

Submitted to the Office of Graduates Studies of
Texas A&M University
in partial fulfillment of the requirements for the degree of

DOCTOR OF PHILOSOPHY

Approved by:

Chair of Committee, Ohannes Eknoyan
Committee Members, Henry F. Taylor
Kai Chang
Gerald Cote
Head of Department, Chanan Singh

December 2005

Major Subject: Electrical Engineering

ABSTRACT

Design and Fabrication of Highly Efficient Electrooptic Modulators Using Bragg Grating Reflectors. (December 2005)

Ryoung-han Kim, B.S., Yonsei University;

M.S., Yonsei University

Chair of Advisory Committee: Dr. Ohannes Eknoyan

Bragg grating reflectors etched in amorphous silicon overlay films have been integrated with Ti:$LiNbO_3$ optical waveguides. With a 12.5 mm long grating segment and an etch depth of ~ 93 nm in a 105 nm-thick silicon film, a narrow (0.05 nm) spectral bandwidth with a record high transmission dip (> 20 dB) was achieved at a wavelength of ~1542 nm for TE polarization on an *x*-cut, *y*-propagating substrate. The reflectance in the channel waveguides is found to be strongly dependent on the depth of the etched grating. The 3-dB bandwidth of 0.05 nm obtained for all tested samples is the smallest reported for waveguides in $LiNbO_3$. The effect of the Bragg waveguide loss factor on the transmittance and reflectance spectra is investigated using a model for contra-directional coupling that includes an attenuation coefficient.

The Bragg grating spectral characteristics are exploited to fabricate distributed Bragg feedback modulators (DBFM) and Bragg reflector Fabry-Perot modulators (BFPM). The sharp cut-off in transmission and reflection spectra, which is an inherent

characteristic of Bragg grating, was tuned by applying voltage via the linear electrooptic effect, to produce intensity modulation.

The Bragg grating based modulators consume less electric power compared to polarization intensity modulators (PIMs). The DBFM demonstrates 1/1.6 times the modulating voltage of a PIM with identical waveguide and electrode structure. The BFPM shows 1/3.3 times the modulating voltage of the PIM. No difference in the frequency response is observed among the three modulators. Comparison of the modulation sensitivity in the linear region indicates that the Bragg grating based modulators provide better sensitivity than that of the PIM with identical waveguide and electrode structure.

These results indicate the potential advantage of the Bragg grating based modulators for enhanced modulation efficiency over conventional modulators. Further improvements can be expected from the optimization of the electrode design.

ACKNOWLEDGMENTS

I would like to thank the many people who have helped me to get through toward this dissertation. I am appreciative to Dr. O. Eknoyan for giving me endless support, motivation, and encouragement by serving as my advisor. He has been and will be my true model for life-long learning. Also I would like to thank to Dr. H. F. Taylor for being my committee member, for having the discussions with me, and giving me huge advice. I have been very fortunate to be with Dr. Eknoyan and Dr. Taylor. Thanks to Dr. K. Chang and Dr. G. Cote for serving as my committee members, for their time and considerations. The help of all of my friends, Yong-wook, Seong-kyu, Myung-joon, Jung-Moo, Pilip, Kuo, Renato, Robert, Jim and Yonsei family members are deeply appreciated. My wife Miney, I owe so much for the years of hard work she had to do for me. I can’t find enough words to express my appreciation to her. Everytime when I have been suffering from the loads, she has cured me like the best medicine, and always reminded me that I am not here alone, we are here together for the one goal. With her, I could make everything that I have right now. To my family, father and mother, my debts are unmeasureable and I dedicate my acheivements to them. They have been my biggest motivation to get over a high mountain named a life. My family-in-laws, especially Younie Huh-who is one of my biggest fans and has always given me a consistant support, strong encouragement, I appreciate so much. God bless you all.

TABLE OF CONTENTS

Page

ABSTRACT iii

ACKNOWLEDGMENTS v

TABLE OF CONTENTS vi

LIST OF FIGURES ix

LIST OF TABLES xiv

CHAPTER

I INTRODUCTION 1

II THEORETICAL REVIEW 5

A. Wave Propagation……. 5
B. Guided Wave Propagation 7
C. Optical Indicatrix in Uniaxial Crystals 9
D. Electrooptic Effect……… 12
E. Waveguide Diffraction by Bragg Grating 15
1. Modeling the Effect of Bragg Waveguide Loss Factor on Spectral Response 18
F. Fabry-Perot Interferometer 20

III DEVICE STRUCTURE AND ANALYSIS 24

A. Electrooptic Phase Modulator 24
B. Polarization Intensity Modulator (PIM) 26
C. Distributed Bragg Feedback Intensity Modulator (DBFM) 30
D. Bragg Reflector Fabry-Perot Modulator (BFPM) 32

IV DEVICE FABRICATION 36

A. Ti:$LiNbO_3$ Channel Waveguide 36
B. Amorphous Silicon Surface-Relief Type Bragg Grating 37
C. Electrode Fabrication… 41

CHAPTER Page

V EXPERIMENTAL RESULTS 42

A. Silicon Bragg Grating 42
B. The Modeling of Bragg Grating Spectra Considering Loss Factor 49
C. Polarization Intensity Modulator (PIM) 56
D. Distributed Bragg Feedback Intensity Modulator (DBFM) 60
E. Bragg Reflector Fabry-Perot Modulator (BFPM) 70
1. Bragg Reflectro Fabry-Perot Modulator (BFPM) with Short Electrodes 78
F. Frequency Response of the Modulators 81
G. Modulation Sensitivity of the Modulators 87

VI CONCLUSIONS 89

VII SUGGESTIONS FOR FUTURE WORK 91

REFERENCES 92

APPENDIX 1 97

APPENDIX 2 99

APPENDIX 3 100

APPENDIX 4 102

APPENDIX 5 104

APPENDIX 6 105

APPENDIX 7 107

APPENDIX 8 108

APPENDIX 9 110

APPENDIX 10 112

APPENDIX 11 114

APPENDIX 12 116

Page

APPENDIX 13 117

APPENDIX 14 118

APPENDIX 15 120

APPENDIX 16 121

APPENDIX 17 125

VITA 126

LIST OF FIGURES

FIGURE Page

2.1 Schematic diagram of a planar waveguide 7

2.2 Index ellipsoid of a uniaxial crystal 11

2.3 Schematic diagram of Bragg gratings on a waveguide............................... 15

2.4 Sample Bragg transmission and reflection spectra. 18

2.5 Model for analyzing a Fabry-Perot effect. 20

2.6 Sample transmission spectrum of a Fabry-Perot interferrometer with a constant mirror reflectance (R=constant). 22

3.1 Schematic diagram of a phase modulator 24

3.2 Schematic diagram of a polarization intensity modulator (PIM)................ 26

3.3 Schematic diagram of a sample modulation of the polarization intensity modulator (PIM). 30

3.4 Schematic diagram of a distributed Bragg feedback intensity modulator (DBFM)... 30

3.5 Schematic representation of modulations in transmission (left) and reflection (right) power of distributed Bragg feedback intensity modulator (DBFM) 32

3.6 Schematic diagram of a Bragg reflector Fabry-Perot modulator (BFPM) .. 32

3.7 Schematic representatoin of modulations in transmission (left) and reflection (right) power of Bragg reflector Fabry-Perot modulator (BFPM). 34

4.1 Schematic diagram of a two-beam interference setup 39

4.2 Schematic drawing of the coplanar electrodes.. 41

5.1 SEM photograph of the silicon grating with a period of about 350 nm 42

FIGURE Page

5.2 Schematic diagram of the setup for broadband spectrum analysis 43

5.3 Erbium-doped fiber (EDF) laser source spectrum on an optical spectrum analyzer (OSA). 44

5.4 Measured broadband transmittance spectrum for TE input polarization from Ti diffused waveguide with 105-nm-thick Si overlay and gratings etched for 20 seconds 45

5.5 Schematic diagram of the setup for a DFB laser spectrum analysis 45

5.6 DFB laser source spectrum on optical spectrum analyzer at T_{TEC}=28.5 ^oC 46

5.7 Transmission and reflection spectra obtained using DFB laser diode that was tuned thermally. Solid line: reflection for a 20 seconds etched sample, dotted line: reflection for an 18 seconds etched sample, and dash-dot line: transmission for an 18 seconds etched sample...................... 47

5.8 Model calculations for the variation of κL and transmission dip assuming no loss ($\alpha = 0$) for different time durations. Solid line: modeled from the program.. 49

5.9 Model calculations for the variation of αL and spectral width between minima for the reflectance peak with κL as a parameter 50

5.10 Spectra obtained for a 16 seconds etched grating sample (solid line: experimental, dash line: model). (a) Transmission, and (b) reflection 52

5.11 Spectra obtained for an 18 seconds etched grating sample (solid line: experimental, dash line: model). (a) Transmission, and (b) reflection 53

5.12 Spectra obtained for a 20 seconds etched grating sample (solid line: experimental, dash line: model). (a) Transmission, and (b) reflection 54

5.13 Test setup for DC and RF modulation of the polarization intensity modulator (PIM) 56

5.14 DC-voltage response of output optical power of the PIM 57

FIGURE Page

5.15 RF polarization intensity modulation of PIM. Upper traces are the optical output and lower traces are the electrical waveform at 1-kHz. (a) Applied peak-to-peak 18 volts (10V/div), and (b) applied peak-to-peak 28.7 volts (10V/div) ... 59

5.16 Broadband EDF transmission spectra obtained for 20 seconds etched DBFM device. (a) Before reducing the segment length (12 mm), and (b) after reducing the segment length (2 mm) ... 61

5.17 Measured narrowband spectra of DBFM for TE input polarization using a thermal tuning of the DBF laser ... 62

5.18 Bragg wavelength shift as a function of applied DC-voltage in DBFM ... 63

5.19 Spectra of Bragg wavelength shift in DBFM by DC-voltage obtained using DFB laser; (a) transmission, and (b) reflection ... 65

5.20 DC-voltage tuning response of DBFM; (a) transmitted, and (b) reflected optical output power ... 67

5.21 RF modulation of DBFM. Upper traces are the optical output and lower traces are the electrical waveform at 1-kHz. (a) Transmission: applied peak-to-peak 8.6 volts (5V/div), (b) transmission: applied peak-to-peak 20 volts (10V/div), (c) reflection: applied peak-to-peak 10 volts (5V/div), and (d) reflection: applied peak-to-peak 20 volts (10V/div) ... 68

5.22 Transmission RF modulation of DBFM. Upper trace is the optical output , and lower trace is the electrical waveform at 1-kHz (10V/div) ... 69

5.23 Broadband EDF transmission spectra obtained for a 20 seconds etched BFPM. (a) Before etching the segment length (12 mm), and (b) after producing Fabry-Perot configuration (each segment is 2 mm, and two segments separated by 3 mm) ... 71

5.24 Narrowband spectra from BFPM for a TE input polarization using the thermal tuning of a DBF laser ... 72

5.25 DC-voltage modulation response of BFPM; (a) transmitted power, and (b) reflected power ... 74

FIGURE Page

5.26 RF modulation of BFPM. Upper traces are the optical output and lower traces are the electrical waveform at 1-kHz. (a) Transmission: applied peak-to-peak 6 volts (5V/div), (b) transmission: applied peak-to-peak 12 volts (5V/div), (c) reflection: applied peak-to-peak 5.5 volts (5V/div), and (d) reflection: applied peak-to-peak 11 volts (5V/div) 76

5.27 Distorted modulation waveform of transmitted power for swiching voltage measurement of BFPM. Upper trace is the optical output and lower trace is the electrical waveform at 1-kHz (5V/div) 77

5.28 Schematic diagram of BFPM with short electrodes 78

5.29 Broadband and narrowband spectra for TE input polarization of BFPM with short electrodes. (a) Broadband spectrum using an EDF, and (b) narrowband spectra using a DFB laser.. 79

5.30 DC-voltage modulation response of BFPM with short electrodes; (a) transmitted power, and (b) reflected power... 80

5.31 Distorted modulation waveform for transmitted power for BFPM with short electrodes. Upper trace is the optical output and lower trace is the electrical waveform at 1-kHz (10V/div) 81

5.32 Equivalent circuit model of a lumped electrode modulator......................... 81

5.33 The simulation result of the effect on the bandwidth and the electrical power across the electrodes by varying the additional resistance................ 83

5.34 Frequency response of the optical power of PIM with and without the 50 Ω additional resistor at the terminal of the probe 84

5.35 Schematic diagram of a photodetector equivalent circuit............................ 85

5.36 Frequency responses of the optical output power of the modulators........... 86

5.37 Normalized peak-to-peak output intensity as a function of normalized applied modulation voltage.. 88

A.1 Schematic diagram of the two plane waves incident on a plane containing *x*-axis 114

FIGURE Page

A.2 Schematic diagram of the intensity variation on the *x*-plane by two beam interference 115

A.3 SEM photographs of (a) photoresist grating pattern, and (b) silicon grating pattern with the silicon film thickness of 1400 Å for 40 seconds at 100 W in RIE-ICP 116

A.4 The LabVIEW™ front panel for the GPIB control and the data acquisition 118

A.5 The LabVIEW™ block diagram for the GPIB control and the data acquisition 119

A.6 Temperature tuning of the DFB laser wavelength 120

A.7 Applied current vs. output power of the DFB laser 120

A.8 Circuit diagram for RF power reduction 125

LIST OF TABLES

TABLE Page

5.1 Reflection and insertion loss dependence on gratings' etch time. All samples are the same length and the same Si overlay film thickness.......... 48

5.2 Calculated values of attenuation α and coupling κ coefficients for gratings produced with different etching duration times............................. 51

A.1 Manufacturer supplied electrical/optical characteristics of the DFB laser at T_{sub}=25°C 117

CHAPTER I

INTRODUCTION

Present communication technology relies on fiber-optic systems which include light sources such as a laser, optical fiber, integrated optical components such as modulators and switches, and optical detectors. The lasers and detectors are fabricated using semiconductor materials, and the integrated optical components are generally fabricated using electrooptic single crystal materials such as lithium niobate ($LiNbO_3$). Among the integrated optical components, the contribution from electrooptic modulators using $LiNbO_3$ waveguide structures has been significant in the last several decades due to their high-speed and chirp-free nature [1]. The essential requirements for efficient electrooptic modulation are low half-wave (switching) voltage and broad 3-dB modulation bandwidth.

Bragg reflection grating is a spatially periodic perturbation of mode indices in the direction of propagation of a guided optical wave and designed to reflect a specific wavelength. To reflect light of a wavelength λ, the refractive index perturbation period Λ must satisfy the Bragg condition $\Lambda = m\ \lambda/2n$, where m is the grating order, λ is the free space optical wavelength at the reflectance peak, and n is the effective refractive index of the guided mode [2] (Chap. 13, pp. 491-539).

This thesis follows the style and format of *IEEE Journal of Lightwave Technology*.

Recently, Bragg reflection gratings have been of interest for integration with optical channel waveguides in lithium niobate ($LiNbO_3$) for the development of various integrated optics devices. These devices include slow-wave electrooptic modulators [3-6], polarization mode dispersion compensators [7], waveguide lasers [8], and several other components that are attractive for wavelength division multiplexed (WDM) network applications. A number of techniques have been used for making Bragg reflection gratings on optical waveguides in $LiNbO_3$, including Ti implantation [9], etched corrugations in a Si overlay film [10], UV-induced surface relief [11], laser ablation [12], and proton exchange [13]. In the 1550 nm wavelength regime, which is of interest for optical networks, the period Λ for first order (m = 1) Bragg reflection is approximately 350 nm. Producing a mask pattern by photolithographic methods with 175 nm (for $\Lambda/2$) spaced lines requires the application of an antireflection coating on the substrate to reduce interference effects due to multiple reflections during the exposure of the photoresist. Moreover, $LiNbO_3$ is very difficult to etch. Such impediments can be alleviated through the use of a silicon (Si) overlay film by virtue of its high optical absorption coefficient at visible wavelengths, and its high transparency near 1550 nm. Also, silicon is much easier to etch [10]. Furthermore, since Si has a refractive index (~ 3.4) that is much larger than that of $LiNbO_3$ (~ 2.2), it is possible to obtain a strong contradirectional coupling via interaction of the evanescent wave of the guided mode with the large-index-difference grating [14]. The contradirectional coupling coefficient κ is a measure of the strength of interaction between the refractive index perturbation and the guided mode. However, the combined effects from modal field redistribution due to

the presence of the high-index overlay film, the complex relative permittivity of Si which at the 1550 nm spectral regime is small but finite [15-17], and the scattering from the Bragg grating introduce a loss factor that must be accounted for in analysis. Moreover, attenuation in optical channel waveguides increases with the thickness of a high-index overlay film in a nonlinear manner [15-17]. In principle, the spectral width for transmission and reflection spectra also depends on κ, but practically it can be affected by absorption loss in the optical waveguide and scattering loss caused by the Bragg grating.

The transmission and reflection spectra from a waveguide with Bragg grating show sharp transitions near the Bragg wavelength. The spectra can be electrically tuned via the electrooptic effect and could lead to intensity modulation. The sharp tunable transitions provide venues for producing low switching voltage modulators. By forming a Fabry-Perot structure with Bragg grating reflector segments, the transitions can be made even sharper, making it possible to produce high sensitivity and lower voltage modulators [18] (Chap. 8, pp. 276-316) [19].

This dissertation reports Bragg grating reflectors which are integrated on $LiNbO_3$ channel waveguide that produce high transmission dip and narrow spectral bandwidth, and two types of $LiNbO_3$ modulators, distributed Bragg feedback intensity modulator (DBFM) and Bragg reflector Fabry-Perot modulator (BFPM), that show lower switching voltages compared to polarization intensity modulator (PIM) of similar dimensions. Bragg reflection grating is the key element which makes the low switching voltage possible in these device configurations. The developed Bragg gratings have a high in-

band rejection and a narrow bandwidth not achieved previously in a Bragg-reflector channel waveguide on a ferroelectric substrate. The effect of the Bragg waveguide loss factor on the transmittance and reflectance spectra is investigated numerically using a model for contradirectional coupling that includes an attenuation coefficient. The DBFM and the BFPM demonstrate themselves as improved electrooptic modulators, and their design and realizations in $LiNbO_3$ are reported for the first time.

CHAPTER II

THEORETICAL REVIEW

A. Wave Propagation

Propagation of electromagnetic waves can be analyzed by Maxwell's equations,

$$\nabla \times \underline{E} = -\frac{\partial \underline{B}}{\partial t} \tag{2.1}$$

$$\nabla \times \underline{H} = \underline{J} + \frac{\partial \underline{D}}{\partial t} \tag{2.2}$$

$$\nabla \cdot \underline{D} = \rho \tag{2.3}$$

$$\nabla \cdot \underline{B} = 0 \tag{2.4}$$

where $\underline{E}$ (V/m) and $\underline{H}$ (A/m) represent electric and magnetic field intensity vectors, $\underline{D}$ (C/m^2) and $\underline{B}$ (T) represent the electric flux density (electric displacement) vector and the magnetic flux density (magnetic displacement) vector, $\underline{J}$ (A/m^2) is the electric current density, and ρ (C/m^2) denotes the electric charge density.

Polarization effects of a medium are related to the electric and magnetic displacement vectors by the constitutive relations,

$$\underline{D} = \varepsilon_o \underline{E} + \underline{P} = \varepsilon \underline{E} \tag{2.5}$$

$$\underline{P} = \varepsilon_o \chi_e \underline{E} \tag{2.6}$$

$$\underline{B} = \mu_o (\underline{H} + \underline{M}) = \mu \underline{H} \tag{2.7}$$

where ε (F/m) is the permittivity of the medium, ε_o is the permittivity of free space ($\varepsilon = \varepsilon_r \varepsilon_o$), χ_e is the electric susceptibility of the medium (unitless), $\underline{P}$ is the electric

polarization (dipole moment per unit volume) of the medium, μ (H/m) is the permeability of the medium, μ_o is the permeability of free space, and $\underline{M}$ is the magnetic polarization (dipole moment per unit volume) of the medium. Assuming a non-magnetic homogeneous dielectric ($\mu = \mu_0, \varepsilon = \varepsilon_0 n^2$) source free ($\underline{J}$ = 0 and ρ = 0) medium, the combination of equations (2.1)-(2.7) and employing the vector identity $\underline{A} \times \underline{B} \times \underline{C} \equiv \underline{B}(\underline{A} \cdot \underline{C}) - \underline{C}(\underline{A} \cdot \underline{B})$ yields

$$\nabla^2 \underline{E}(r,t) - \frac{n^2}{c^2} \frac{\partial^2 \underline{E}}{\partial t^2} = 0, \tag{2.8}$$

where c is the speed of light in vacuum. Considering a monochromatic wave oscillating at a radian frequency of $\omega \left(= \frac{2\pi c}{\lambda} \right)$, the electric field $\underline{E}$ can be expressed in a form of

$$\underline{E}(r,t) = \underline{E}(r) e^{-j\omega t}. \tag{2.9}$$

Therefore, equation (2.8) can be written as

$$\nabla^2 \underline{E}(r) + k_o^2 n^2 \underline{E}(r) = 0 \tag{2.10}$$

where k_o ($=\omega/c$) is the free space propagation constant of light, and n is the refractive index of the medium. Supposing that the plane wave propagates along z-direction with a propagation constant β, the electric field equation then can be expressed by

$$\underline{E}(r,t) = \underline{E}(x,y) e^{-j(\omega t - \beta z)} \tag{2.11}$$

and inserting equation (2.11) into (2.10) gives,

$$\left(\frac{\partial^2}{\partial x^2} + \frac{\partial^2}{\partial y^2} \right) \underline{E}(x,y) + (k_o^2 n^2 - \beta^2) \underline{E}(x,y) = 0. \tag{2.12}$$

B. Guided Wave Propagation

The channel waveguide model in which the dimensions are finite in both *x*- and *y*- directions can be explained with a planar waveguide (Fig. 2.1) model with a small error factor. The wave behavior inside the channel waveguide is modified with a simple quantitative method when a planar waveguide model is converted into a channel waveguide model [20] (Chap. 3, pp. 32-46).

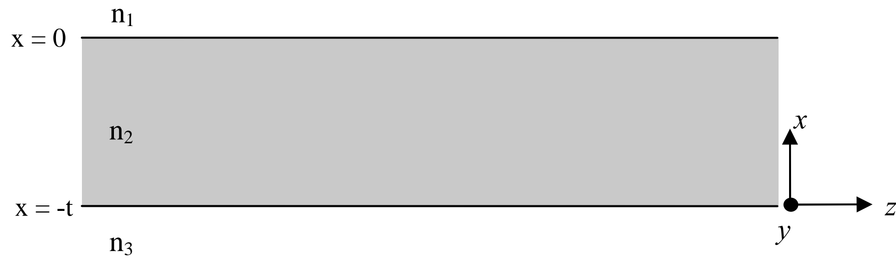

Figure 2.1 Schematic diagram of a planar waveguide.

The wave propagates only in the middle region (n_2) by the total internal reflection (TIR) without scattering into n_1 or n_3 region ($n_2 > n_1$, n_3). The wave equation of the planar waveguide which does not have an electric field variation in *y*-direction is

$$\frac{d^2}{dx^2}E(x) + (k_o^2 n_i^2 - \beta^2)E(x) = 0 \qquad (2.13)$$

where *E(x)* is either an *x* or *y* directed field amplitude of $\underline{E}(x)$ vector and n_i is the refractive index in each region. Considering a TE polarization (i.e. polarized along *y*-axis) of the light which is propagating along *z*-axis, the field component can be expressed as

$$\underline{E}(r,t) = E_y(x)e^{-j(\omega t - \beta z)} \cdot \hat{a}_y \,. \tag{2.14}$$

To have guided modes in the n_2 region and decaying modes in the n_1 and n_3 regions, the transverse function $E_y(x)$ in equation (2.14) should be written in the form of

$$E_y(x) = \begin{cases} Ae^{-qx} & x > 0 \\ B\cos(hx) + C\sin(hx) & -t \le x \le 0 \\ De^{-p(x+t)} & x < -t \end{cases} \tag{2.15}$$

where *A, B,* and *C* are arbitrary constants, *t* is the thickness of the planar waveguide, and $q = \sqrt{\beta^2 - k_0^2 n_1^2}$, $h = \sqrt{k_0^2 n_2^2 - \beta^2}$, and $p = \sqrt{\beta^2 - k_0^2 n_3^2}$.

By applying the boundary condition in which the tangential field components E_y and H_z should be continuous at both $x = 0$ and $x = -t$, one can obtain an eigenvalue equation as

$$\tan(ht) = \frac{p+q}{(h - \frac{q}{h}p)} \,. \tag{2.16}$$

This eigenvalue equation is used to find the eigenvalue β for confined modes inside the waveguide and restrict the solution to only finite numbers of guided modes that can possibly exist inside the waveguide.

A similar approach is applied for the case of TM polarization, the field component is

$$\underline{H}(r,t) = H_y(x)e^{-j(\omega t - \beta z)} \cdot \hat{a}_y \,. \tag{2.17}$$

Treating the transverse function in the same manner and using the boundary conditions, the eigenvalue equation for TM mode is given by

$$\tan(ht) = \frac{\left(\frac{n_2}{n_1}\right)^2 q + \left(\frac{n_2}{n_3}\right)^2 p}{h - \left(\frac{n_2^2}{n_1 n_3}\right)\frac{pq}{h}} . \qquad (2.18)$$

C. Optical Indicatrix in Uniaxial Crystals

Optical indicatrix is an ellipsoid whose intercepts are determined by the refractive indices and the crystal orientation. In an isotropic medium, the permittivity ε in equation (2.5) is a constant scalar. However, because the induced polarization by applied electric field can have different values along each axis, the permittivity in an anisotropic medium becomes tensor [ε] and equation (2.5) can be expressed in the forms of

$$\underline{D} = \begin{bmatrix} D_x \\ D_y \\ D_z \end{bmatrix} = \begin{bmatrix} \varepsilon_{11} & \varepsilon_{12} & \varepsilon_{13} \\ \varepsilon_{21} & \varepsilon_{22} & \varepsilon_{23} \\ \varepsilon_{31} & \varepsilon_{32} & \varepsilon_{33} \end{bmatrix} \cdot \begin{bmatrix} E_x \\ E_y \\ E_z \end{bmatrix} . \qquad (2.19)$$

By rotating axes, the permittivity tensor [ε] can be diagonalized as

$$[\varepsilon] = \begin{bmatrix} \varepsilon_{11} & 0 & 0 \\ 0 & \varepsilon_{22} & 0 \\ 0 & 0 & \varepsilon_{33} \end{bmatrix} \qquad (2.20)$$

where ε_{11}, ε_{22}, and ε_{33} are called the principle permittivities.

The electric energy density of an electromagnetic wave is given by

$$U_e = \frac{1}{2}\underline{E} \cdot \underline{D} . \qquad (2.21)$$

For an anisotropic-diagonalized system,

$$U_e = \frac{1}{2}\left(\varepsilon_{11}E_x^2 + \varepsilon_{22}E_y^2 + \varepsilon_{33}E_z^2\right) \\ = \frac{1}{2}\left(\frac{D_x^2}{\varepsilon_{11}} + \frac{D_y^2}{\varepsilon_{22}} + \frac{D_z^2}{\varepsilon_{33}}\right) \quad . \tag{2.22}$$

By defining the quantities *X*, *Y*, and *Z* as the units measured along three principle axes such that $X = D_x / \sqrt{2U_e\varepsilon_o}$, $Y = D_y / \sqrt{2U_e\varepsilon_o}$, and $Z = D_z / \sqrt{2U_e\varepsilon_o}$, equation (2.22) can be expressed as

$$\frac{X^2}{(\varepsilon_{11}/\varepsilon_o)} + \frac{Y^2}{(\varepsilon_{22}/\varepsilon_o)} + \frac{Z^2}{(\varepsilon_{33}/\varepsilon_o)} = 1 . \tag{2.23}$$

The values of the denominator in equation (2.23) can be transformed into the refractive indices of the medium along each principle axis:

$$\frac{X^2}{n_x^2} + \frac{Y^2}{n_y^2} + \frac{Z^2}{n_z^2} = 1 \tag{2.24}$$

where n_x, n_y, and n_z are the refractive indices along each principle axes. This equation is called "*Index ellipsoid equation*" or "*optical indicatrix equation*" and is used to determine the optical properties of a crystal. In a *uniaxial* medium ($n_x = n_y \neq n_z$) which includes tetragonal, trigonal and hexagonal crystallographic systems, the index ellipsoid is rotationary symmetrical with respect to the *z*-axis, which is called the optic axis. The index ellipsoid of a uniaxial crystal is depicted following the index ellipsoid equation in Fig. 2.2.

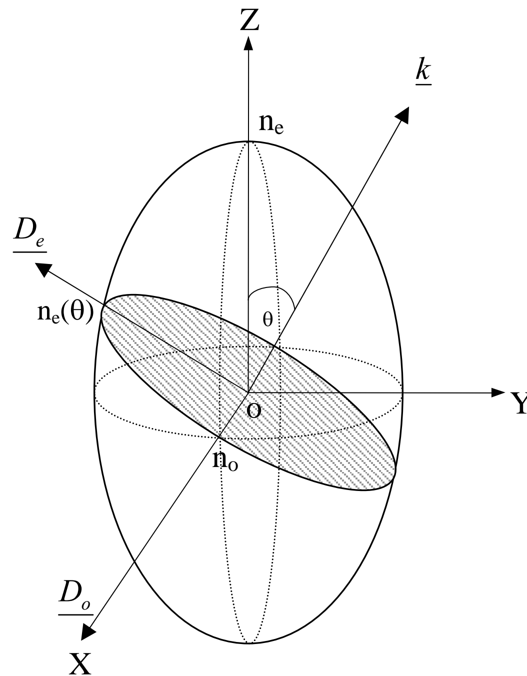

Figure 2.2 Index ellipsoid of a uniaxial crystal.

Consider that the light is propagating in $\underline{k}$ direction in the uniaxial crystal shown in Fig. 2.2. To find the allowed light polarization and the refractive indices that the polarizations see, an intersecting ellipse plane which is normal to $\underline{k}$ (The shaded region in Fig. 2.2) can be drawn. From this ellipse, two orthogonal polarizations which have directions to $\underline{D_o}$ and $\underline{D_e}$ are identified. One allowed polarization directed along $\underline{D_o}$ experiences the refractive index n_o which is independent of the angle θ. The other allowed polarization directed along $\underline{D_e}$ experiences the index $n_e(\theta)$, which depends on

angle θ. The wave polarization in which the refractive index is angle independent is called "*ordinary wave*" and the other one which is angle dependent is called "*extraordinary wave*." The index of the extraordinary wave can be calculated by the intersection length in Fig. 2.2 which is expressed as [2] (Chap. 1, pp. 1-38),

$$n_e(\theta) = \frac{n_0 n_e}{\sqrt{n_e^2 \cos^2\theta + n_0^2 \sin^2\theta}} . \tag{2.25}$$

It can be seen easily from equation (2.25) that the uniaxial crystal behaves as an isotropic crystal if the light is incident along the optic z-axis.

D. Electrooptic Effect

The propagation of an electro-magnetic wave inside a medium is determined by the refractive index of the medium. The electrooptic effect is the change of refractive index with application of electric field [21] (Chap. 5, pp. 96-129).

In an anisotropic material without an inversion symmetry, the polarization of the medium can be changed linearly proportional to an external applied electric field. This phenomenon is called a linear electrooptic effect (*Pockels effect*); otherwise, in a centrosymmetrical crystal, the linear electrooptic effect doesn't appear, while the non-linear electrooptic effect (*Kerr effect*) can be observed. Because the linear electrooptic effect produces a much larger refractive index change than the non-linear electrooptic effect when a voltage is applied, it is used in most integrated optic devices. In the case of an anisotropic material such as $LiNbO_3$, the induced index change along ellipsoid axes

depends on the polarity of the voltage applied to the crystal. The undiagonalized index ellipsoid equation can be expressed as

$$\left(\frac{1}{n^2}\right)_1 x^2 + \left(\frac{1}{n^2}\right)_2 y^2 + \left(\frac{1}{n^3}\right)_3 z^2 + 2\left(\frac{1}{n^2}\right)_4 yz + 2\left(\frac{1}{n^2}\right)_5 xz + 2\left(\frac{1}{n^2}\right)_6 xy = 1 \quad (2.26)$$

By choosing x, y, and z to be parallel to the principle axes of the crystal, equation (2.26) reduces to

$$\frac{X^2}{n_x^2} + \frac{Y^2}{n_y^2} + \frac{Z^2}{n_z^2} = 1. \quad (2.27)$$

The index change induced by an applied electric field E^e is defined by

$$\Delta\left(\frac{1}{n^2}\right)_i = \sum_{j=1}^{3} r_{ij} E_j^e \quad (2.28)$$

where E_j^e is the amplitude of the applied electric field, and r_{ij} is the linear electrooptic coefficient tensor. Expressing equation (2.28) in a matrix form,

$$\begin{bmatrix} \Delta\left(\frac{1}{n^2}\right)_1 \\ \Delta\left(\frac{1}{n^2}\right)_2 \\ \Delta\left(\frac{1}{n^2}\right)_3 \\ \Delta\left(\frac{1}{n^2}\right)_4 \\ \Delta\left(\frac{1}{n^2}\right)_5 \\ \Delta\left(\frac{1}{n^2}\right)_6 \end{bmatrix} = \begin{bmatrix} r_{11} & r_{12} & r_{13} \\ r_{21} & r_{22} & r_{23} \\ r_{31} & r_{32} & r_{33} \\ r_{41} & r_{42} & r_{43} \\ r_{51} & r_{52} & r_{53} \\ r_{61} & r_{62} & r_{63} \end{bmatrix} \cdot \begin{bmatrix} E_1 \\ E_2 \\ E_3 \end{bmatrix} . \quad (2.29)$$

The crystal symmetry defines the value of r_{ij}. For the case of $LiNbO_3$, the electrooptic tensor is [21] (Chap. 5, pp. 96-129)

$$r_{ij} = \begin{bmatrix} 0 & -r_{22} & r_{13} \\ 0 & r_{22} & r_{13} \\ 0 & 0 & r_{33} \\ 0 & r_{51} & 0 \\ r_{51} & 0 & 0 \\ -r_{22} & 0 & 0 \end{bmatrix} \tag{2.30}$$

where r_{33} = 30.8 × 10^{-12} m/V, r_{13} = 8.6 × 10^{-12} m/V, r_{22} = 3.4 × 10^{-12} m/V, and r_{51} = 26 × 10^{-12} m/V [22] (Chap. 9, pp.222-246). Because r_{33} has the largest value among the electrooptic coefficients of $LiNbO_3$, most electrooptic devices in $LiNbO_3$ are designed to use the r_{33} electrooptic coefficient. By restricting the application of the electric field along the z-axis, the index ellipsoid equation in a uniaxial crystal system such as $LiNbO_3$ becomes

$$\left(\frac{1}{n_0^2} + r_{13}E_z\right)x^2 + \left(\frac{1}{n_0^2} + r_{13}E_z\right)y^2 + \left(\frac{1}{n_e^2} + r_{33}E_z\right)z^2 = 1. \tag{2.31}$$

Since the index changes related to the applied electric field are significantly small (i.e. $\left|r_{13}n_0^2E_z\right|$ << 1, and $\left|r_{33}n_e^2E_z\right|$ <<1), it is possible to expand each refractive indices under the applied field using Taylor's expansion. By taking the first two biggest terms,

$$\begin{aligned} n_x &= n_0 - \frac{1}{2}n_0^3 r_{13}E_z \\ n_y &= n_0 - \frac{1}{2}n_0^3 r_{13}E_z \\ n_z &= n_e - \frac{1}{2}n_e^3 r_{33}E_z \end{aligned} \tag{2.32}$$

.

As indicated in equation (2.32), the electrooptic effect enables the phase, intensity and polarization of the light inside the waveguide to be controlled by an electric field.

E. Waveguide Diffraction by Bragg Grating

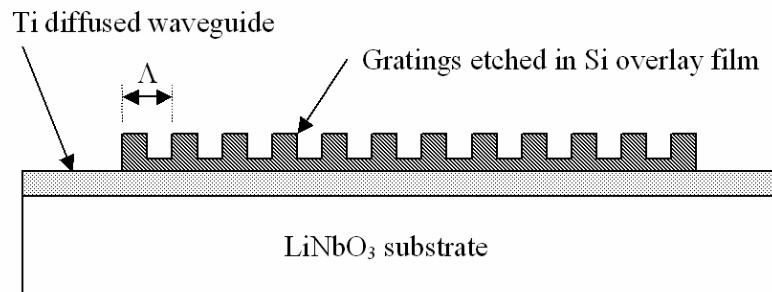

Figure 2.3 Schematic diagram of Bragg gratings on a waveguide.

Figure 2.3 shows the geometry of the Bragg gratings on a waveguide. By periodic surface corrugation, numbers of partial mirror reflectors are introduced in the waveguide. As the wave travels in the periodic structure, it experiences reflection at each mirror along its path. This introduces modes coupling between forward and backward traveling waves through the length of the grating. The coupling efficiency depends on the spatial period of the grating Λ, the optical wavelength of the wave λ, the effective index of the wave mode n_{eff}, and the coupling coefficient κ. According to the coupled mode theory [2] (Chap.13, pp. 491-539), most efficient coupling between forward and

backward traveling waves occurs when the phase matching condition is satisfied. The phase matching condition (= Bragg diffraction condition) is given by

$$\Lambda = \frac{m\lambda}{2n_{eff}} \tag{2.33}$$

where Λ is the period of the grating, m is the grating order, λ is the wavelength and n_{eff} is the effective index of the waveguide. Denoting the amplitude of the forward propagating mode by A and that of the backward propagating mode by B, then the coupled mode equation can be expressed as [2] (Chap.13, pp. 491-539),

$$\frac{dA}{dy} = \kappa_{ab} B e^{-i\Delta \cdot y} \tag{2.34-a}$$

$$\frac{dB}{dy} = \kappa_{ba} A e^{-i\Delta \cdot y} \tag{2.34-b}$$

where κ is the coupling coefficient, and Δ is the deviation from the phase matching condition. The κ and Δ are expressed as

$$\kappa = \frac{i\omega\varepsilon_o a_l}{4} \int_{-\infty}^{\infty} \Delta n^2(x) \left[\mathrm{E}_z^{(s)}(x) \right]^2 dx\,, \tag{2.35}$$

and

$$\Delta = \beta_a - \beta_b \pm \frac{2\pi}{\lambda} = \frac{4\pi n_{eff}}{\lambda} - \frac{2\pi}{\Lambda}\,. \tag{2.36}$$

where β_a and β_b are the propagation constants for the counter propagating modes. The fundamental feature of the waveguide Bragg grating is that an incident mode is most effectively reflected at the wavelength which satisfies the Bragg diffraction condition (i.e. Bragg wavelength λ_{Bragg}). Theoretically, the wavelength far from the Bragg wavelength

has transmission with no loss. In other words, the waveguide Bragg grating acts as a narrow band filter for the wavelength which satisfies the Bragg condition. Solving the coupled mode equation with the boundary condition $A(0)=1$ and $B(L)=0$ for an incident wave with a grating segment length L, a power reflectivity can be obtained.

When 2κ>Δ, the power reflectivity can be expressed as

$$R = |A(0)|^2 == \frac{4\kappa^2 \sinh^2\left(\frac{SL}{2}\right)}{\Delta^2 \sinh^2\left(\frac{SL}{2}\right) + S^2 \cosh^2\left(\frac{SL}{2}\right)} \tag{2.37}$$

where $S = \sqrt{4\kappa^2 - \Delta^2}$, and $\kappa = |\kappa_{ab}|$. When 2κ<Δ, it can be written as

$$R = \frac{4\kappa^2 \sin^2\left(\frac{PL}{2}\right)}{\Delta^2 \sin^2\left(\frac{PL}{2}\right) + P^2 \cos^2\left(\frac{PL}{2}\right)} \tag{2.38}$$

where $P = \sqrt{\Delta^2 - 4\kappa^2}$.

Figure 2.4 shows the sample transmittance and reflectance spectra for an ideal Bragg grating structure with λ_{Bragg}=1542 nm.

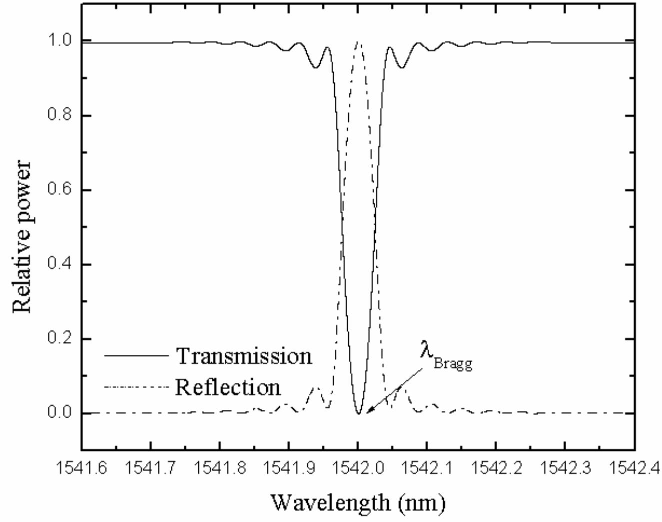

Figure 2.4 Sample Bragg transmission and reflection spectra.

1. Modeling the Effect of Bragg Waveguide Loss Factor on Spectral Response

It is assumed that the waveguide is a single mode, propagation is along the *y*-axis, and the Bragg grating order $m = 1$. To account for the effect of the Bragg waveguide loss factor on the transmission and reflection spectral responses, the coupled mode equations for contradirectional coupling are modified as

$$\frac{dA}{dy} = \kappa B e^{i\Delta y} - \alpha A \tag{2.39-a}$$

$$\frac{dB}{dy} = \kappa A e^{-i\Delta y} + \alpha B . \tag{2.39-b}$$

In these equations, α is the amplitude attenuation coefficient which is equal to half the power attenuation coefficient. Expanding the complex field amplitudes into their real

and imaginary components $A = A_r + iA_i$, $B = B_r + iB_i$, and $e^{\pm i\Delta y}$ as $[\cos(\Delta y) \pm i\sin(\Delta y)]$, the incremental changes in the real and imaginary components of the field amplitudes over a distance Δy are obtained as

$$\Delta A_r = [\kappa B_r \cos(\Delta y) - \kappa B_i \sin(\Delta y) - \alpha A_r]\Delta y \quad (2.40a)$$

$$\Delta A_i = [\kappa B_i \cos(\Delta y) + \kappa B_r \sin(\Delta y) - \alpha A_i]\Delta y\,, \quad (2.40b)$$

and

$$\Delta B_r = [\kappa A_r \cos(\Delta y) + \kappa A_i \sin(\Delta y) + \alpha B_r]\Delta y \quad (2.41a)$$

$$\Delta B_i = [\kappa A_i \cos(\Delta y) - \kappa A_r \sin(\Delta y) + \alpha B_i]\Delta y\,. \quad (2.41b)$$

Equations (2.40a) - (2.41b) can be solved numerically using the finite difference method to calculate the complex field amplitudes with α and κ as input parameters, and normalized boundary conditions $(A_r) = 1$, $(A_i) = 0$ and $(B_r) = (B_i) = 0$ at the exit of the Bragg waveguide segment. The reflectance and transmittance spectra can be obtained from the normalized amplitudes magnitude $|B|^2$ and $|A|^2$ at the terminals of the waveguide.

The values of κ and α for an experimental sample can be determined from the model calculations by using the measured dip in the transmission spectrum and the bandwidth between minima of the sample's reflectance peak spectrum. For a fixed value of κ, the analysis indicates that in a lossless case ($\alpha = 0$), the spectral width between the first two reflectance minima on either side of the peak is equal to the spectral width of the first two transmittance maxima relative to the dip. However, for a lossy case ($\alpha \neq 0$)

the values of such spectral widths are different for the transmittance and reflectance spectra, and the difference increases with α.

F. Fabry-Perot Interferometer

A Fabry-Perot interferometer makes use of multiple reflections inside a resonant cavity which consists of two partial mirrors [23] (Chap.4, pp. 101-152).

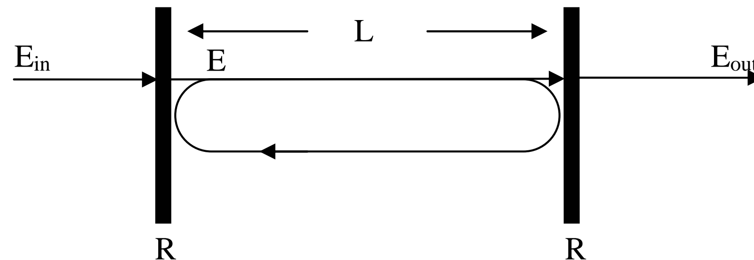

Figure 2.5 Model for analyzing a Fabry-Perot effect.

In Figure 2.5, R, E_{in}, E and E_{out} denote the power reflectivity (= the reflectance of each of the two mirrors), the input electric field amplitude, the field amplitude inside the cavity, and the output electric field amplitude, respectively. By applying the input electric field with amplitude E_{in} to the first mirror,

$$E = \sqrt{1-R} \cdot E_{in} \,. \tag{2.42}$$

After one round trip of the wave inside the cavity, the electric field E becomes the sum of reflected and incident waves,

$$E = \sqrt{1-R} \cdot \sqrt{R} \cdot \sqrt{R} \cdot e^{i\phi} E_{in} + \sqrt{1-R} \cdot E_{in} \tag{2.43}$$

where ϕ is the round trip phase shift $\phi = \frac{4\pi nL}{\lambda}$. After two round trips,

$$E = E_i \sqrt{1-R} (1 + \mathrm{Re}^{i\phi} + R^2 e^{2i\phi}) . \tag{2.44}$$

With N round trips,

$$E = E_i \sqrt{1-R} \sum_{n=0}^{N} a^n \tag{2.45}$$

where $a = \mathrm{Re}^{i\phi}$. For steady state, i.e. for infinite number of round trips, the electric field amplitude can be expressed by

$$E = E_{in} \sqrt{1-R} \sum_{n=0}^{\infty} a^n = E_{in} \sqrt{1-R} \frac{1}{1-a} . \tag{2.46}$$

By adding the partial waves at the output to get the total outgoing wave E_{out}, we obtain

$$E_{out} = \left(E_{in} \sqrt{1-R} \frac{1}{1-a} \right) \cdot \sqrt{1-R} . \tag{2.47}$$

The transmittance of the Fabry-Perot cavity is defined by

$$T_{power} = \frac{E_{out} \cdot E_{out}^*}{\left| E_{in} \right|^2} = \frac{(1-R)^2}{\left| 1-a \right|^2} = \frac{(1-R)^2}{1 + R^2 - 2R \cdot \cos\phi} . \tag{2.48}$$

A sample transmittance spectrum with R as a constant for all wavelengths is shown in Fig. 2.6.

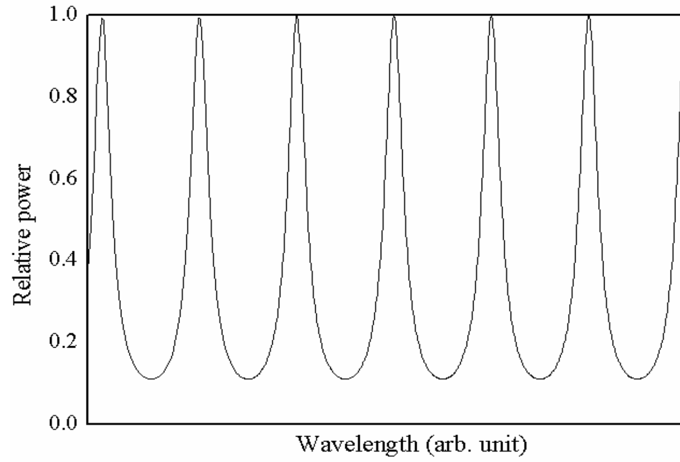

Figure 2.6 Sample transmission spectrum of Fabry-Perot interferometer with a constant mirror reflectance (R=constant).

The characteristics of the Fabry-Perot cavity are often expressed by the free spectral range (FSR) and finesse *F*. The free spectral range is defined by the wavelength (or frequency) difference between the two adjacent peaks. The free spectral range in terms of wavelength is

$$\Delta\lambda_{FSR} = \frac{\lambda^2}{2n_{eff}L} \tag{2.49}$$

where λ is the wavelength of the light in free space, n_{eff} is the effective index of the waveguide, and *L* is the cavity length. The finesse is a measure of the sharpness of slope which is defined as [24] (Chap. 7, pp. 256-367),

$$F = \pi\frac{\sqrt{R}}{(1-R)}\,. \tag{2.50}$$

The relative transmitted power in terms of the finesse becomes

$$T_{power} = \frac{1}{1 + 4\left(\frac{F}{\pi}\right)^2 \cdot \sin^2 \varphi} \qquad (2.51)$$

where R is the reflectivity of the mirror and φ $\left(= \frac{1}{2}\phi = \frac{2\pi nL}{\lambda}\right)$ is the half-round trip phase shift.

CHAPTER III

DEVICE STRUCTURE AND ANALYSIS

A. Electrooptic Phase Modulator

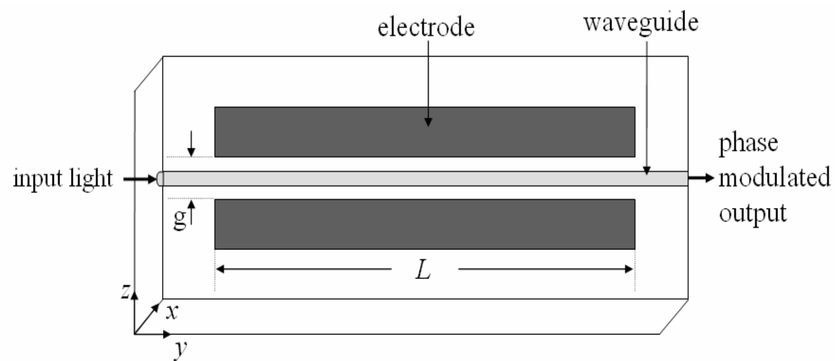

Figure 3.1 Schematic diagram of a phase modulator.

The phase modulator is the simplest type of an electrooptic modulator. A conventional channel waveguide phase modulator is shown in Fig. 3.1. Titanium is diffused to form a higher refractive index region in the substrate, and the diffused area (waveguide) is designed to hold a single mode for both TE and TM polarizations. To utilize the largest electrooptic coefficient r_{33}, x-cut and y-propagation configuration of the $LiNbO_3$ substrate is used and an electric field is applied along the z-axis through a pair of coplanar electrodes alongside of the waveguide.

The optical field of TE polarized light which is propagating in the y-direction can be expressed by

$$\underline{E} = E_o \cdot e^{-j(\omega t - \beta y)} \cdot \hat{a}_z \tag{3.1}$$

where $\beta\left(= \dfrac{2\pi n}{\lambda}\right)$ is the propagation constant of the light. The phase shift of the light induced by the applied electric field can be obtained from the linear electrooptic equation (2.35),

$$\Delta\phi = \frac{\pi L}{\lambda} n_e^3 r_{33} E_z^e = \frac{\pi L}{\lambda} n_e^3 r_{33} \frac{V}{g} \tag{3.2}$$

where L is the interaction length between the electric field and the optical field, V is the applied voltage, and g is the gap distance between the electrodes. However, equation (3.2) assumes that the electric field applied to the waveguide is uniform across the waveguide and invariant to the length of the field-applied region. A field overlap integral factor Γ which is always less than the unity should be introduced to account for the spatial field distributions [21] (Chap. 5, pp. 96-129) and is given by,

$$\Gamma = \frac{\iint f^e(y,z) \cdot E_z^2(y,z)dydz}{\iint E_z^2(y,z)dydz}. \tag{3.3}$$

In the above equation, $f^e(y,z)$ represents the applied electric field spatial distribution, and $E_z(y,z)$ is the spatial field distribution of the guided optical wave.

Consequently, the induced phase change is given by

$$\Delta\phi = \frac{\pi L}{\lambda} n_e^3 r_{33} E_z^e \Gamma = \frac{\pi L}{\lambda} n_e^3 r_{33} \frac{V}{g} \Gamma. \tag{3.4}$$

A commonly used figure of merit for electrooptic modulators is the half-wave voltage V_π which is defined as the voltage required to produce an electrooptic phase shift of π. From equation (3.4), the half-wave voltage is

$$V_\pi = \frac{\lambda}{n_e^3 r_{33} \Gamma} \left(\frac{g}{L} \right). \tag{3.5}$$

B. Polarization Intensity Modulator (PIM)

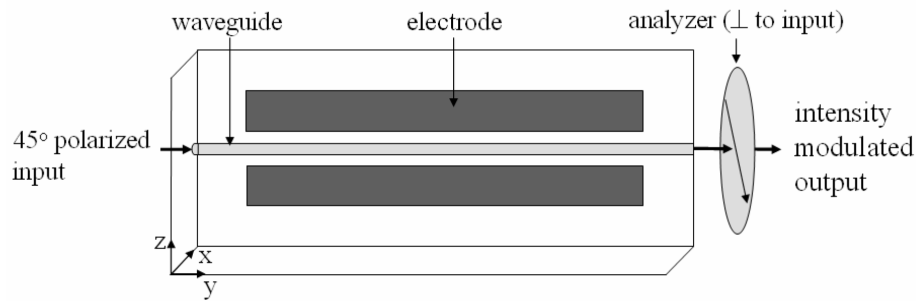

Figure 3.2 Schematic diagram of a polarization intensity modulator (PIM).

The electrooptic phase modulator can be easily converted to the polarization intensity modulator (PIM), as shown in Fig. 3.2. The incident light polarization has an angle of +45º relative to *z*-axis so as to have both TE and TM polarization components simultaneously. And an analyzer (polarizer) is placed at the output of the crystal at an angle of -45º relative to the *z*-axis. Application of the electric field across the electrodes induces different refractive index changes along each axis which leads to different relative phase retardations between TE and TM polarizations and gives rise to the

resulting polarization change. The output polarizer at - 45º relative to the z-axis converts the phase modulation to the intensity modulation by the application of voltage. The input optical wave which has both TE and TM fields can be expressed as

$$\underline{E}_{in}^{w} = \frac{\left|E_i^w\right|}{\sqrt{2}} \cdot \hat{a}_x + \frac{\left|E_i^w\right|}{\sqrt{2}} \cdot \hat{a}_z \ . \tag{3.6}$$

At the output of the waveguides, the optical field is written as

$$\underline{E}_{out}^{w} = \frac{\left|E_i^w\right|}{\sqrt{2}} \cdot e^{j\omega t} \left\{ e^{-jk_o(n_o+\Delta n_o)L} \cdot \hat{a}_x + e^{-jk_e(n_e+\Delta n_e)L} \cdot \hat{a}_z \right\} \tag{3.7}$$

where ω is the angular frequency, k is the wave number, L is the interaction length, and Δn is the index change caused by the applied electric field. The optical field transmitted through the analyzer can be expressed as

$$\underline{E}_{anal}^{w} = \frac{\left|E_i^w\right|}{\sqrt{2}} \cdot e^{j\omega t} \left\{ e^{-jk_o(n_o+\Delta n_o)L} \cdot \hat{a}_x + e^{-jk_e(n_e+\Delta n_e)L} \cdot \hat{a}_z \right\} \cdot \left\{ \frac{1}{\sqrt{2}} \hat{a}_x - \frac{1}{\sqrt{2}} \hat{a}_z \right\}$$

$$= \frac{\left|E_i^w\right|}{2} \cdot e^{j\omega t} \left\{ e^{-jk_o(n_o+\Delta n_o)L} - e^{-jk_e(n_e+\Delta n_e)L} \right\}. \tag{3.8}$$

The output light intensity normalized by the input light intensity is given by

$$\begin{aligned} \frac{I}{I_o} &= \frac{\underline{E}_{anal}^{w} \cdot \underline{E}_{anal}^{w*}}{\left|E_i^w\right|^2} = \frac{\left|\underline{E}_{anal}^{w}\right|^2}{\left|E_i^w\right|^2} \\ &= \frac{1}{2} \cdot \left[1 - \cos\left\{ k_o (n_e - n_o + \Delta n_e - \Delta n_o) L \right\} \right] \\ &= \frac{1}{2} \cdot \left[1 - \cos\left\{ \phi + \Delta\phi \right\} \right] \end{aligned} \tag{3.9}$$

where ϕ is the phase retardation inside the waveguide, and $\Delta\phi$ is the relative phase retardation due to the electric field application. As a result, the total phase retardation by application of voltage is

$$\begin{aligned}\phi_{total} &= \phi + \Delta\phi \\ &= \kappa_o (n_o - n_e)L + \frac{1}{2}\kappa_o (n_e^3 r_{33} - n_o^3 r_{13}) E_z L \cdot \Gamma \\ &= \kappa_o (n_o - n_e)L + \frac{1}{2}\kappa_o n_e^3 r_c E_z L \cdot \Gamma \\ &= \kappa_o (n_o - n_e)L + \frac{1}{2}\kappa_o n_e^3 r_c \frac{V}{g} L \cdot \Gamma\end{aligned} \tag{3.10}$$

where r_c is the effective electrooptic coefficient and is defined as

$$r_c = r_{33} - \left(\frac{n_0}{n_e}\right)^3 r_{13}\,. \tag{3.11}$$

The half-wave voltage V_π which is defined by the amount of voltage required to produce a π-radian phase change in equation (3.10) is obtained as

$$V_\pi = \frac{\lambda g}{n_e^3 r_c \Gamma L}\,. \tag{3.12}$$

Hence equation (3.9) can be rewritten as

$$\frac{I_o}{I_i} = \frac{1}{2}\left\{1 - \cos\left(\phi_o + \pi\frac{V}{V_\pi}\right)\right\} \tag{3.13}$$

where $\phi_o = \kappa(n_o - n_e)L$.

For an efficient modulation, the modulator is generally biased to the quadratic point with DC-voltage, and a small RF voltage is applied as $V = V_{dc} + V_m \sin\omega_m t$. At the

quadratic point, $\phi_o + \pi \frac{V_{dc}}{V_\pi} = \frac{\pi}{2}$ and the ratio of output to incident power with a small RF voltage becomes

$$\frac{I_o}{I_i} = \frac{1}{2}\left\{1 + \sin\pi\left(\frac{V_m \sin\omega_m t}{V_\pi}\right)\right\}. \tag{3.14}$$

For the very small modulating voltage V_m compared to V_π , equation (3.14) can be rewritten as

$$\frac{I_o}{I_i} = \frac{1}{2}\left\{1 + \pi\frac{V_m \sin\omega_m t}{V_\pi}\right\}. \tag{3.15}$$

The modulation depth Δ is proportional to the slope in the linear region and can be expressed as

$$\Delta = \pi\frac{V_m}{V_\pi}. \tag{3.16}$$

Equation (3.16) shows that the output transmitted intensity is linearly proportional to the amplitude of the radio-frequency (RF) modulating voltage $V_m \sin\omega_m t$ [18] (Chap. 8, pp. 276-316). A sample modulation of ideal PIM is illustrated in Fig. 3.3.

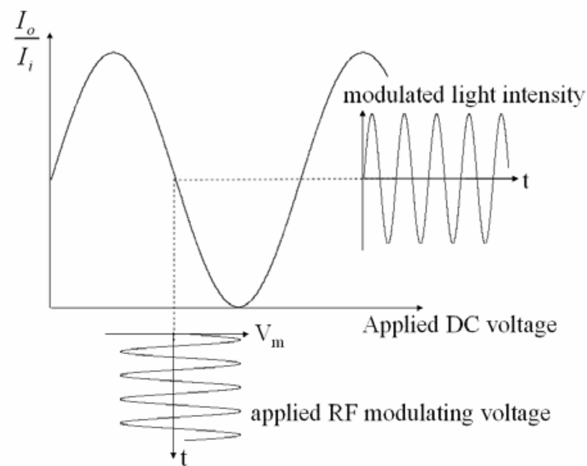

Figure 3.3 Schematic diagram of a sample modulation of the polarization intensity modulator (PIM).

C. Distributed Bragg Feedback Intensity Modulator (DBFM)

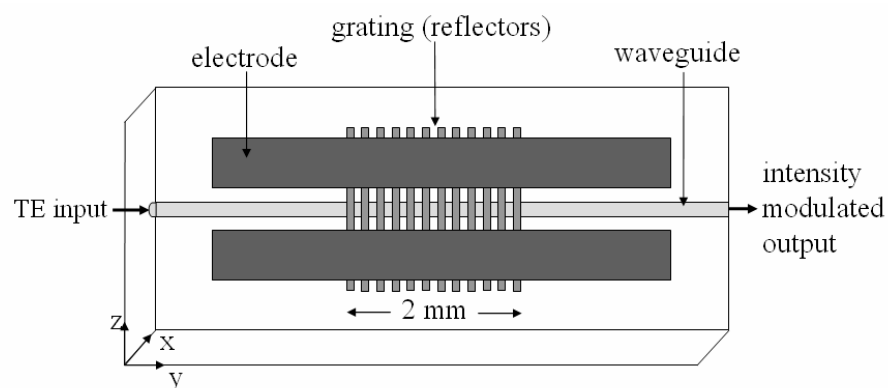

Figure 3.4 Schematic diagram of a distributed Bragg feedback intensity modulator (DBFM).

A schematic diagram of a distributed Bragg feedback intensity modulator (DBFM) having a periodically corrugated surface overlay film is shown in Fig. 3.4. The modulator consists of Bragg gratings on top of the channel waveguide and co-planar electrodes alongside of the waveguide. In the case of the Bragg grating modulation, the input wave polarization is set to TE or TM mode because both see different refractive indices in an anisotropic material and therefore the Bragg diffraction conditions for each mode are different. For a given applied voltage, the effective index inside the waveguide varies due to the linear electrooptic effect. Because the Bragg condition is a function of the effective index, the Bragg wavelength is also tuned by the applied voltage. Using the linear electrooptic effect in equation (2.35), the shifted Bragg wavelength λ'_{Bragg} after application of voltage for a TE polarized optical input can be expressed as

$$\begin{aligned} \lambda'_{Bragg} &= \lambda_{Bragg} + \Delta\lambda_{Bragg} \\ &= \Lambda \cdot 2 \cdot \left(n_{eff} + \frac{1}{2} n_{eff}^{3} r_{33} \frac{V}{g} \cdot \Gamma \right) \end{aligned} \tag{3.17}$$

where r_{33} is the electrooptic coefficient (= 30.8×10^{-12} m/v) along the z-axis of a $LiNbO_3$ crystal, V is the applied voltage, g is the electrode separation gap, and Γ is the fields overlap integral factor. Tuning of the Bragg wavelength gives rise to change in transmittance of the guided light at its given wavelength. By applying appropriate DC bias and small RF voltage as shown previously for PIM, the transmitted light intensity can be modulated. Figure 3.5 shows output intensity modulation in a DBFM.

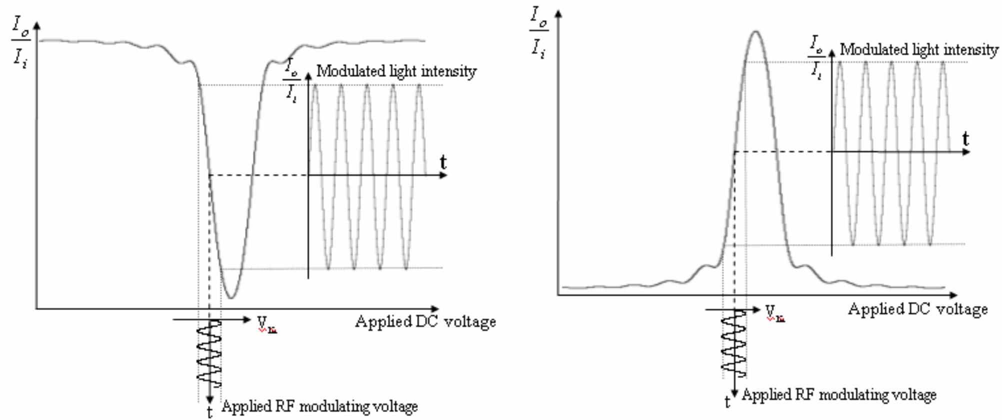

Figure 3.5 Schematic representation of modulations in transmission (left) and reflection (right) power of distributed Bragg feedback intensity modulator (DBFM).

D. Bragg Reflector Fabry-Perot Modulator (BFPM)

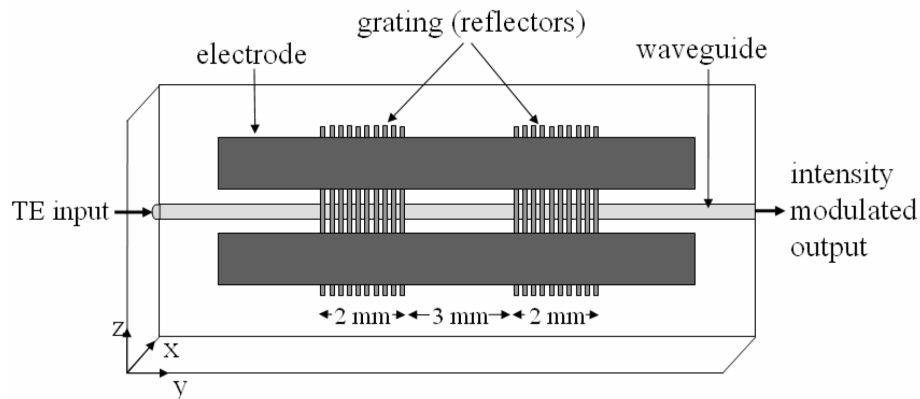

Figure 3.6 Schematic diagram of a Bragg reflector Fabry-Perot modulator (BFPM).

The schematic drawing of a Bragg reflector Fabry-Perot modulator (BFPM) is shown in Fig. 3.6. A conventional Fabry-Perot interferometer integrated in $LiNbO_3$ has been fabricated by depositing thin films of higher refractive index at the end faces of the waveguide [25]. However, the BFPM is designed to replace the end face mirrors with the Bragg grating segments which are fabricated on the waveguide. The Bragg reflectors on the waveguide have the advantages of ease in fabrication, controllability in cavity length by standard photolithographic and microelectronic processes, and demonstration of the potential as a mid-product for a slow-wave optical modulator for very high frequency modulation [4]. It should be noted that one Bragg grating segment in the BFPM act only as a partial mirror reflector for the wavelength which satisfies the Bragg condition so that the strong Fabry-Perot effect appears only near a Bragg wavelength.

As described in Chapter II-F, the transmittance and reflectance of Fabry-Perot interferometer at a certain wavelength are determined by the phase shift which the incident light experiences inside the cavity. Because the round trip phase shift is a function of the effective index which can be controlled by an applied voltage, intensity modulation by application of voltage can be realized.

Figure 3.7 illustrates modulation in transmission and reflection of Bragg reflector Fabry-Perot modulator (BFPM).

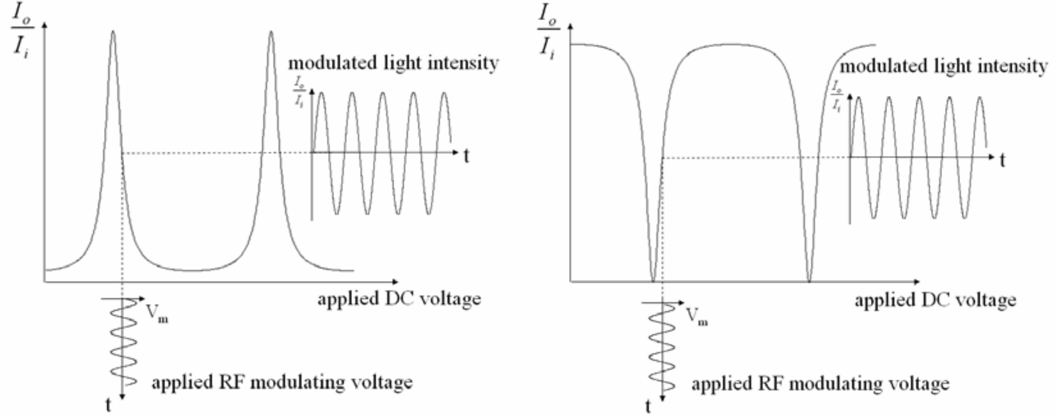

Figure 3.7 Schematic representation of modulations in transmission (left) and reflection (right) power of Bragg reflector Fabry-Perot modulator (BFPM).

Like other modulators, BFPM is also operated by biasing midway of the transmission (or reflection) with appropriate DC-voltage and applying a small RF modulating voltage ($V = V_{dc} + V_m \sin \omega_m t$). When a small modulating voltage is applied, the transmittance in equation (2.51) can be transformed as [18] (Chap. 8, pp.276-316),

$$T_{power} = \frac{1}{1+4\left(\frac{F}{\pi}\right)^2 \cdot \sin^2 \varphi_t\left(V\right)} = \frac{1}{1+4\left(\frac{F}{\pi}\right)^2 \cdot \sin^2\left(\varphi_o + \frac{\pi}{2}\frac{V}{V_\pi}\right)}. \tag{3.18}$$

where V_π is defined as the voltage required to produce the π-radian phase difference which is given by

$$V_\pi = \frac{\lambda g}{n_{eff}^3 r_{33} \Gamma L}. \tag{3.19}$$

By biasing the BFPM at midway (50%) of the transmission, the slope of the transmission curve at the half-transmission point is found by differentiating T_{power} by V/V_{π} which is expressed as [18] (Chap. 8, pp.276-316),

$$\frac{dT_{power}}{d\left(V/V_{\pi}\right)} = F\,. \tag{3.20}$$

Equation (3.20) indicates a modulation depth Δ is proportional to

$$\Delta = F\frac{V_m}{V_{\pi}}\,. \tag{3.21}$$

Whereas PIM has the constant modulation slope π for small modulation voltage, the Fabry-Perot type modulator has the slope F which is theoretically a function of the mirror reflectivity. This indicates that BFPM can potentially have a higher modulation sensitivity with an appropriate choice of the mirror reflectance. In view of voltage consumption, this leads to more efficient modulation compared to PIM.

CHAPTER IV

DEVICE FABRICATION

A. Ti:$LiNbO_3$ Channel Waveguide

The channel waveguides are fabricated by diffusing titanium strips into x-cut $LiNbO_3$ crystals. To produce a modulator with a large depth of modulation, the waveguides were designed to be single mode. This was achieved by an appropriate choice of diffusion parameters such as width and thickness of titanium strips, diffusion time and temperature.

Starting with a 3-inch diameter, 1-mm thick *x*-cut $LiNbO_3$ wafer (Crystal Technology Inc.), sample cutting produced 12 mm x 16 mm samples (see Appendix 1). After the cleaning process (see Appendix 2), a titanium (Ti) film of thickness 1050 Å with errors of ± 20 Å was deposited on the surface of substrate using a DC-sputter (see Appendix 3). In order to generate a Ti strip pattern, a positive photolithography process (see Appendix 4) was carried out using Clariant AZ 5214 as a photoresist. After patterning a 7 μm wide photoresist channel on the substrate, hard-baking at 135 ^{o}C for 5 minutes followed. Defining a photoresist pattern edge was performed using an O_2 plasma ashing process (see Appendix 5). To transfer the photoresist pattern into the Ti film, a reactive ion etching (RIE) process was used (see Appendix 6). In order to avoid the substrate damage due to RIE over-etching, a thin layer of Ti film was left after RIE etching. Wet etching by a DI-water diluted hydrofluoric (HF) acid solution (1:20 ratio by volume) removed the thin layer [26]. After the wet etch process, the substrate was

immersed in a heated photoresist stripper (Clariant AZ300T) at a temperature of 92 ºC for 15 minutes to totally remove the photoresist. An optical microscope and a surface stylus profiler (Dektak[3]) were used to measure the width and the thickness of the Ti strip pattern, respectively.

A high temperature Ti diffusion (1,025 ºC for ~13 hours) was carried out after acquiring the desired width and thickness of the Ti strip (see Appendix 7). Wet breathing air was flowed during the diffusion process to prevent lithium out-diffusion which can cause an unwanted planar waveguide on the surface [27]. The parameters such as the thickness of Ti strip, the diffusion temperature and the time were optimized in order to get a single mode channel waveguide with a low propagation loss for both TE and TM modes.

After the diffusion process, end facets of the waveguide were optically polished (see Appendix 8) in order to allow a fiber-to-waveguide (butt) coupling. For minimal coupling loss, a good optical finish with 90º edges is critical [28].

B. Amorphous Silicon Surface-Relief Type Bragg Grating

An e-beam evaporation method (see Appendix 9) was used to deposit silicon film on $LiNbO_3$. To make a transferred grating pattern in silicon overlay, photoresist gratings were generated on the surface of the silicon film using a holographic exposure technique with the 459 nm line from an argon-ion laser. Because the desired grating has a line width of 175 nm, i.e. a period of 350 nm, the sensitivity and thickness of a photoresist become very important factors for such a high resolution lithography. For the purpose of

high resolution, Shipley S1805 photoresist was chosen instead of Clariant AZ 5214 photoresist because Shipley S1805 photoresist has a relatively higher sensitivity to the wavelength of 459 nm and generates thickness of around 5000 Å at 5000 rpm, 30 seconds spinning condition while Clariant AZ 5214 is more sensitive to UV light and makes 1.5 μm thick photoresist film. To enhance the resolution, the photoresist was diluted with a solvent of Hochest AZ 1500 thinner (1-methoxy-2-propyl acetate) by volume ratio of 1:2. 1-methoxy-2-propyl acetate was chosen because it is the same solvent which is contained in Shipley S1805 and the addition has the effect of reducing the viscosity of the photoresist which results in a thinner photoresist film after the spinning. The volume mixing of the photoresist with the solvent was chosen to produce near 2000 Å photoresist film which is sufficiently thin to generate ~ 170 nm width of lines and thick enough to withstand in RIE-ICP during silicon film etching. For good adhesion of the photoresist on the silicon film, an adhesion promoter (Clariant, Model AZ 17178523329) was spun prior to the photoresist deposition.

A periodic grating pattern was then defined in the photoresist film by a holographic technique using the 459 nm line from an argon-ion laser (Spectra-Physics, Model BeamLok^{TM}, see Appendix 10). For the setup, the optical components were carefully chosen to minimize losses of the laser beam. To enhance the resolution, a vibration isolated optical table was used for the setup. A filtered laminar flow hoods was installed above the table to minimize effects from dust particulates.

A schematic description of the two-beam holographic interference setup is shown in Fig. 4.1.

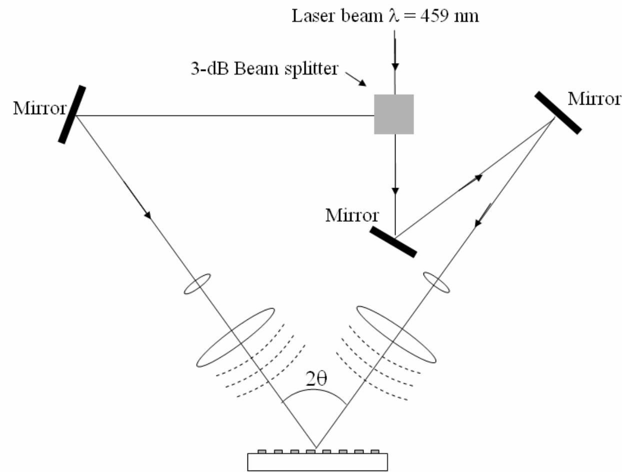

Figure 4.1 Schematic diagram of a two-beam interference setup.

The beam from the Ar gas laser is split by a 3-dB beam splitter, reflected by mirrors and directed to the sample surface with equal and opposite angles of ±θ. The propagation distances of the two beams were set the same to give them the same incident phase.

By the interference of the two plane-waves, a periodic light intensity variation appears along the photoresist. The period of the resultant beam interference pattern on the photoresist is given by (see Appendix 11)

$$\Lambda = \frac{\lambda}{2}\sin\theta . \tag{4.1}$$

The laser beam has a Gaussian power distribution. To give uniform energy distribution over the photoresist film, the beam was expanded to a large size (~ 10 cm

diameter) and collimated in front of the sample. This process is very important in avoiding local over- or under-exposure of the photoresist. However, the optimized duration of the exposure increased as much as 4 minutes due to weak power on the surface of the sample resulting from beam expansion. After exposure, the photoresist was developed using diluted Shipley MF320 (MF320 : DIW = 1 : 0.5 by volume) for about 30 seconds and hard-baked at 135 ^{o}C for 5 minutes. O_2 plasma ashing of the photoresist was then performed for 30 seconds at 100 watts to remove residual photoresist at the bottom of the opened lines of the photoresist pattern. The delineated photoresist pattern was used as a mask to etch spatially periodic corrugations into the Si film. The etching was performed by a reactive ion etching with inductively coupled plasma (RIE-ICP) using a mixture of C_4F_4 and He gas at an RF power of 100 watts. Samples were etched for different durations to control the grating depths. During the etching process, the ends of the waveguides were protected by glass slides over a length of ~ 1 mm. The photoresist of the etched sample was stripped out in a heated photoresist stripper (Clariant AZ300T) at a temperature of 92 ℃ for 5 minutes.

After fabrication of the gratings, another positive photo-lithography process was carried out to form the desired shapes of grating segment for the DBFM and the BFPM. To transfer the photoresist pattern onto the silicon grating, a wet Si etching solution of HNO_3:HF:H_2O (5:1:5 by volume ratio) for a few seconds was used.

C. Electrode Fabrication

Figure 4.2 shows the schematic drawing of the coplanar electrode pattern.

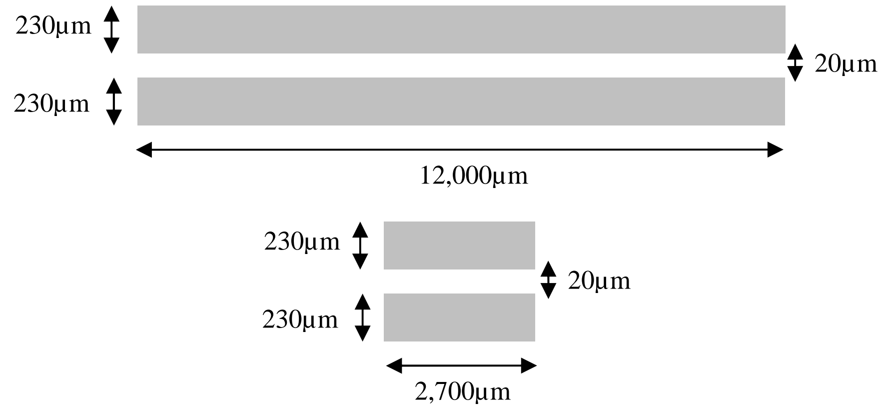

Figure 4.2 Schematic drawing of the coplanar electrodes.

To make a negative photoresist pattern using the positive photoresist, an image reversal photolithography process was used (see Appendix 4). After making the electrode pattern, chromium with thickness of 500 Å, and aluminum with thickness of 3,000 Å were deposited consecutively by electron beam evaporation (see Appendix 9) onto the patterned photoresist openings on the surface of the substrate while monitoring the thickness of the metal films using a thickness monitor. The chromium layer was used to improve the adhesion of the metal to the surface of the substrate. After the deposition process, the lift-off process inside a sonicated acetone bath was used to get the desired electrode pattern.

CHAPTER V

EXPERIMENTAL RESULTS

A. Silicon Bragg Grating

A scanning electron microscope (SEM) was used to check the morphology of the gratings. A SEM picture of a grating etched in a 105-nm-thick Si film for 20 s is shown in Fig. 5.1.

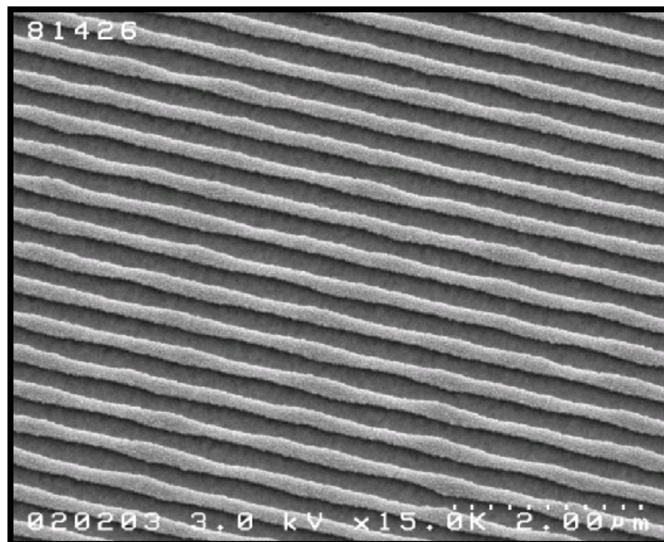

Figure 5.1 SEM photograph of the silicon grating with a period of about 350 nm.

To act as an absorption layer which prevents the reflection from the silicon-$LiNbO_3$ interface and the back surface of the $LiNbO_3$, the silicon film should be sufficiently thick. The jagged lines indicate the presence of some reflections during

exposure due to the insufficient Si film thickness (~105 nm) for the absorption of 459 nm wavelength visible light. However, nearly perfect uniform straight-line patterns were obtained on samples with a thicker (more than 1400 Å) Si film but needed longer RIE-ICP etching time (see Appendix 12).

Transmission spectra for waveguides with gratings were first tested using the amplified spontaneous emission from an erbium-doped fiber (EDF) as a broadband light source and monitoring the output on an optical spectrum analyzer (Anritsu, Model MS9710C). The test and measurement setup is shown in Fig. 5.2.

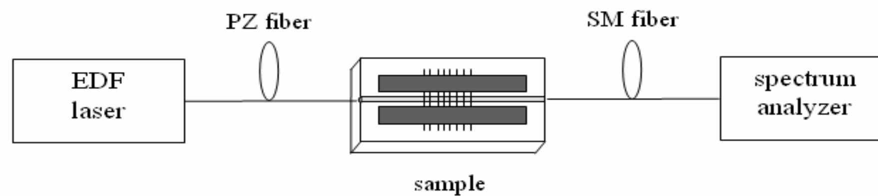

Figure 5.2 Schematic diagram of the setup for broadband spectrum analysis.

In order to obtain a broadband spectrum, the polarized light wave from the polarization fiber (PZ fiber) is coupled to the waveguide. At the output side of the waveguide, a single mode fiber (SM fiber) is directed to the spectrum analyzer to monitor and display the spectrum. The EDF source spectrum is depicted in Fig. 5.3, which indicates the broadband spectrum of the source covers from ~1520 nm to ~1570 nm wavelength range.

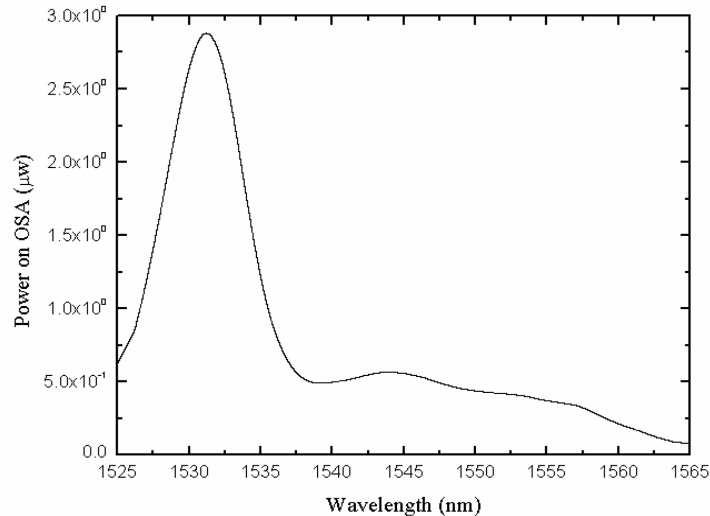

Figure 5.3 Erbium-doped fiber (EDF) laser source spectrum on an optical spectrum analyzer (OSA).

Figure 5.4 shows a relative broadband transmittance spectrum with > 20 dB dip for TE input polarization from a waveguide with a 105-nm-thick Si overlay and 93 nm deep gratings that were etched for 20 s. For TM polarization, the Bragg reflection wavelength falls outside the spectrum of the EDF because it experiences a different refractive index. The relative power in Fig. 5.4 represents the fiber-to-fiber insertion loss, with butt-coupled single mode fibers at the input and output of the waveguide. The loss is about ~ 15.6 dB on the longer wavelength side of the transmission dip, and ~ 3.5 dB greater on the shorter wavelength side. The higher loss at shorter wavelengths is attributed to phase-matched coupling into radiation modes.

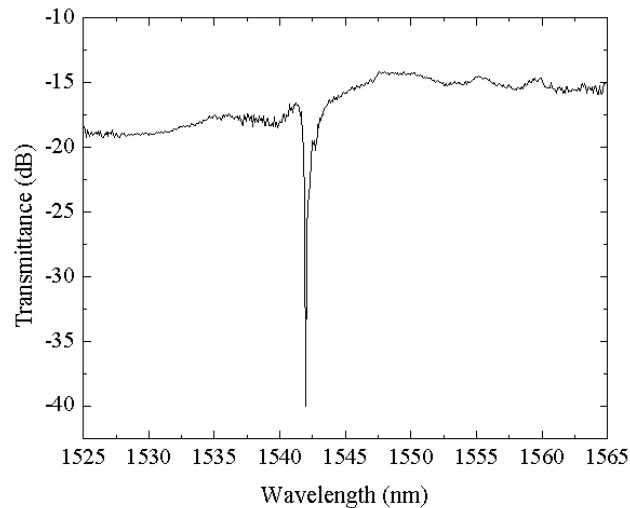

Figure 5.4 Measured broadband transmittance spectrum for TE input polarization from Ti diffused waveguide with 105-nm-thick Si overlay and gratings etched for 20 seconds.

Further optical characterization was carried out by a butt coupling from a pigtailed DFB laser diode (NTT, Model NLK1556STG-BX) using a thermal tuning of the laser wavelength (see Appendix 13). The test setup is illustrated in Fig. 5.5.

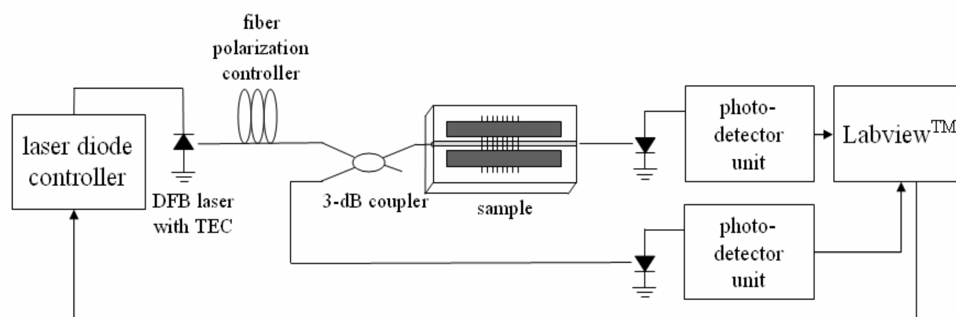

Figure 5.5 Schematic diagram of the setup for a DFB laser spectrum analysis.

Input polarization is set to TE using a fiber polarization controller. The transmitted light power is measured by guiding the output light from the waveguide to the photodetector through a butt-coupling of the single mode fiber. The reflected power passes a 3-dB coupler and the output fiber is directed to the photodetector. With LabVIEW™ (National Instruments, Version 6.0) software (see Appendix 14) programming, the laser diode controller (ILX Lightwave, Model LDC-3724B) was remotely controlled by computer to tune the thermoelectric cooler (TEC) of the DFB laser at a constant rate, and the reading on the power meter was set to be acquired simultaneously. The GPIB (National Instruments, Model 183617K-01) and NI-DAQ™ (National Instruments, Model BNC-2090) boards were used to interconnect the laser diode controller and power meter to the computer, respectively.

The source spectrum of the DFB laser on the optical spectrum analyzer is depicted in Fig. 5.6.

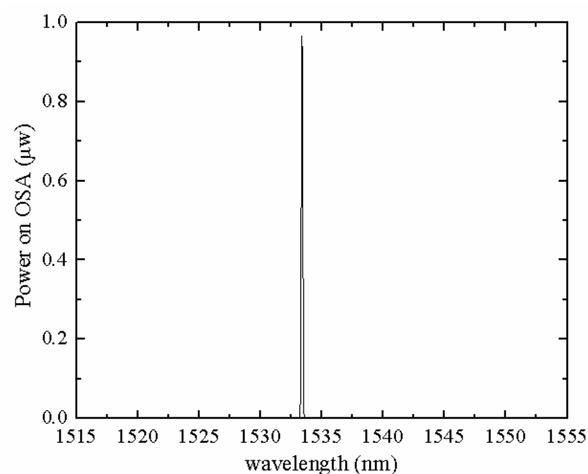

Figure 5.6 DFB laser source spectrum on optical spectrum analyzer at T_{TEC}=28.5 ^{o}C.

Due to its monochromatic nature, the DFB laser is more spectrally sensitive and therefore more suitable for narrow band spectrum analysis than the EDF laser. Further details of the DFB laser characteristics on current and temperature are in Appendix 15. The laser output power was fixed at 1 mW during the experimental measurements.

The reflection spectrum obtained with the DFB laser diode setup from the same waveguide as in Fig. 5.4 is shown as the solid line in Fig. 5.7. For comparison, transmission and reflection spectra from a waveguide in another sample that was produced by etching the gratings for 18 s through a similar 105-nm-thick Si overlay film are also shown in Fig. 5.7.

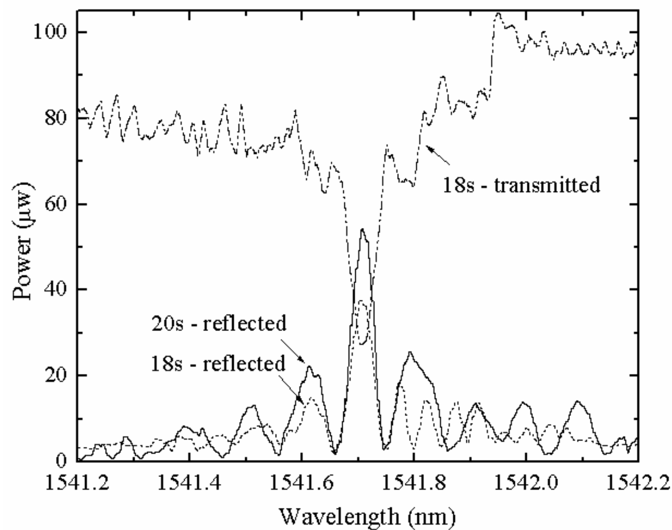

Figure 5.7 Transmission and reflection spectra obtained using DFB laser diode that was tuned thermally. Solid line: reflection for a 20 seconds etched sample, dotted line: reflection for an 18 seconds etched sample, and dash-dot line: transmission for an 18 seconds etched sample.

From the Figure 5.7, the 18 seconds etched sample clearly indicates a lower reflection relative to the 20 seconds etched sample, which indicates longer etching produces stronger diffraction. The 3-dB bandwidth for all of the spectra in Fig. 5.7 is ~ 0.05 nm, which to our knowledge is the smallest reported for waveguides in $LiNbO_3$. The measured values for reflection and insertion loss from three samples with gratings that were formed by different etching times are shown in Table 5.1.

Table 5.1 Reflection and insertion loss dependence on gratings' etch time. All samples are the same length and the same Si overlay film thickness.

Etch time (s)	Reflection (%)	Insertion loss (dB)
16	50	5.4
18	75	6.6
20	> 99	15

The 3-dB bandwidth for each was ~ 0.05 nm. All three samples had identical Si overlay film thickness of 105 nm and lengths (12-mm) of grating segment. The insertion loss of waveguides in each sample for TE input polarization before etching the gratings was 4.2 dB. As noted, longer etching times produced stronger reflections from the deeper gratings.

B. The Modeling of Bragg Grating Spectra Considering the Loss Factor

The finite difference method for the modeling of Bragg grating spectra considering the loss factor was carried out using a computer generated simulation (see Appendix 16). Values for κL and αL were determined by fitting experimental data to the calculated transmittance and reflectance spectra.

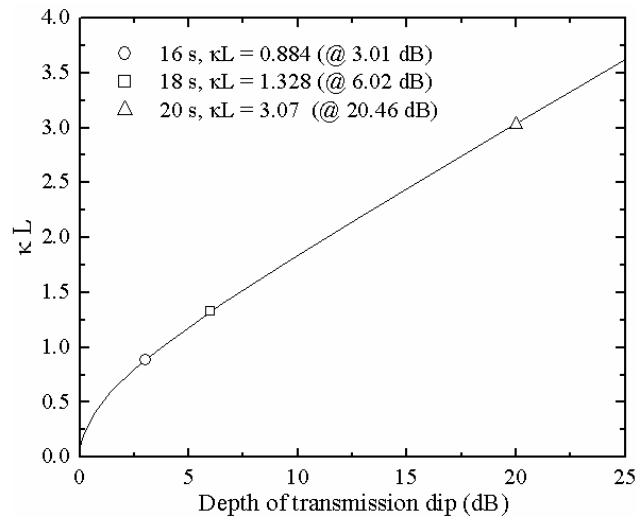

Figure 5.8 Model calculations for the variation of κL and transmission dip assuming no loss (α = 0) for different time durations. Solid line: modeled from the program.

The solid line in Fig. 5.8 represents the simulation result of κL as a function of the depth of the transmission dip assuming no loss (α = 0). This assumption can be justified because the effect of loss coefficient α on coupling coefficient κ is negligibly small. The values for κL for each etching time were obtained from Fig. 5.8 using the

measured depth of the transmission dip of each tested sample as an input parameter. The values for αL are then deduced from Fig. 5.9, which is produced from the model with each κL values corresponding to those obtained for each sample, using the measured spectral width between the first two minima of the reflectance peak for the Bragg waveguide on that sample as an input.

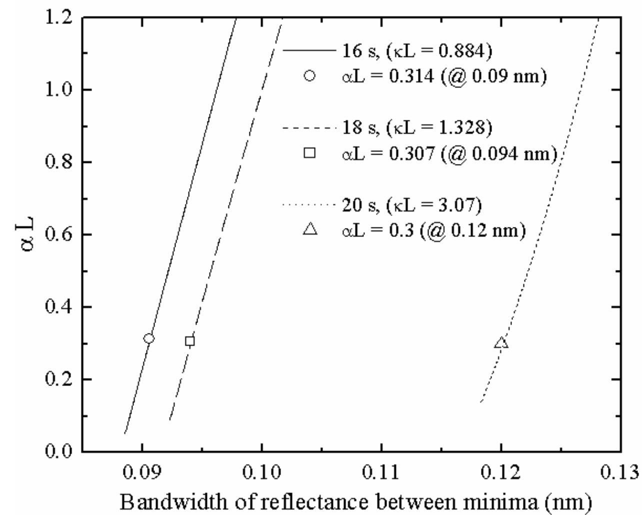

Figure 5.9 Model calculations for the variation of αL and spectral width between minima for the reflectance peak with κL as a parameter.

The values obtained for the attenuation coefficients α and coupling coefficients κ are listed in Table 5.2. The higher values of κ for samples with the longer etch time (deeper corrugations) support the observed larger experimental transmission dip in such samples as those in Table 5.1, and the nearly constant attenuation α indicates that the

grating waveguide loss is due primarily to field redistribution and absorption in the Si film rather than scattering from the grating.

Table 5.2 Calculated values of attenuation α and coupling κ coefficients, for gratings produced with different etching duration times.

Etch duration (s)	Attenuation coefficient α (mm^{-1})	Coupling coefficient κ (mm^{-1})
16	0.0251	0.071
18	0.0246	0.106
20	0.0240	0.246

The latter is also verified by the slightly lower α values in the deeper etched samples, indicating a reduced effective film thickness.

With those determined κL and αL values, the curve fitting between modeled and experimental spectra was carried out. The solid line curves in Figs. 5.10, 5.11, and 5.12 are the transmission (set "a") and reflection (set "b") spectra obtained with the thermally tuned DFB laser diode from the Bragg waveguides that were produced by etching the gratings for durations of 16 s, 18 s and 20 s, respectively. They reveal the increase in reflectivity with increased etching time, as expected due to the larger index perturbation for the deeper etched corrugations. The dashed lines in Figs. 5.10, 5.11, and 5.12

represent the numerical results for output spectra obtained by using the determined values of κL and αL in each sample, as described above.

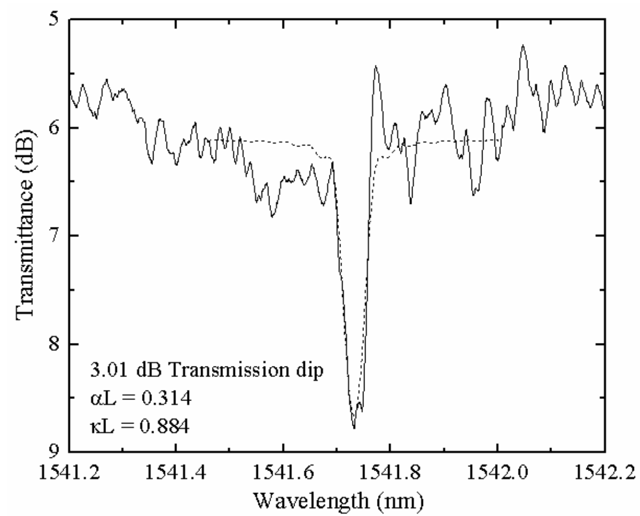

(a)

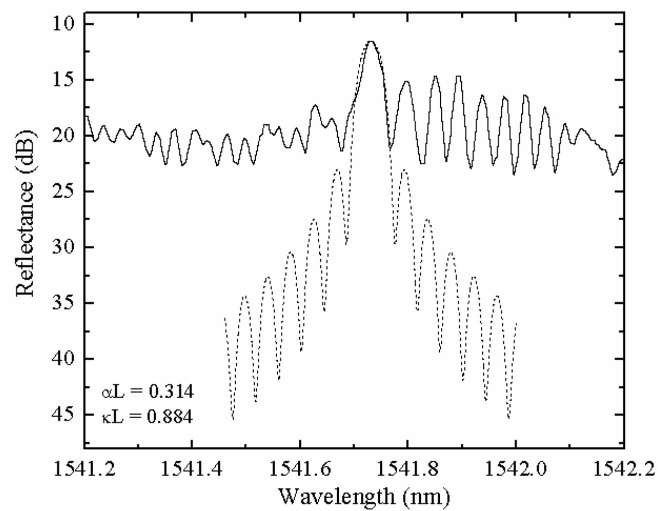

(b)

Figure 5.10 Spectra obtained for a 16 seconds etched grating sample (solid line: experimental, dash line: model). (a) Transmission, and (b) reflection.

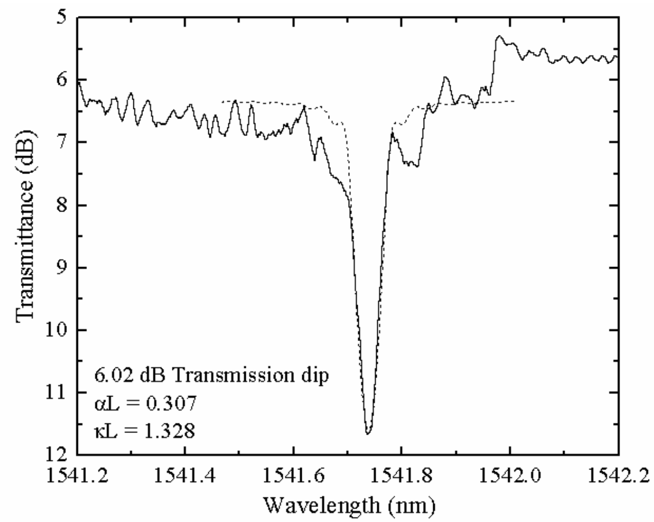

(a)

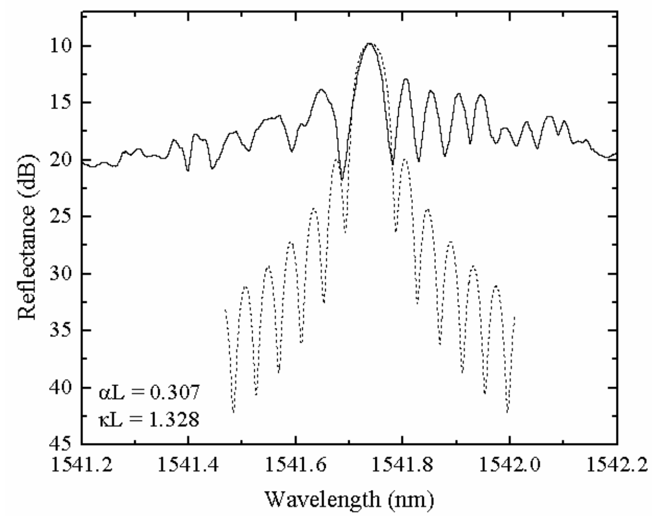

(b)

Figure 5.11 Spectra obtained for an 18 seconds etched grating sample (solid line: experimental, dash line: model). (a) Transmission, and (b) reflection.

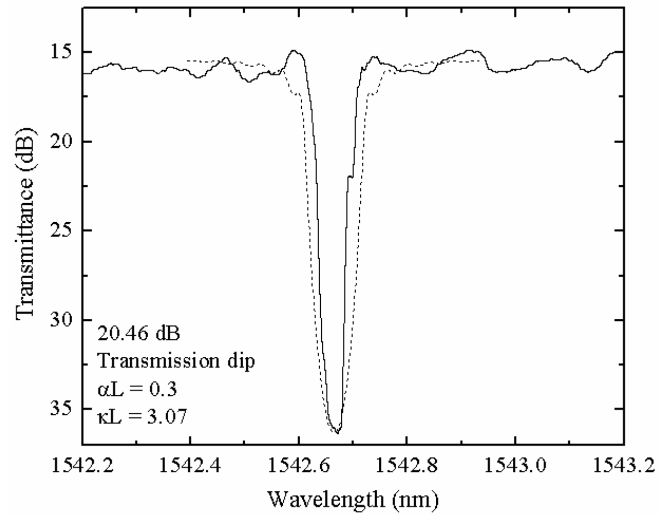

(a)

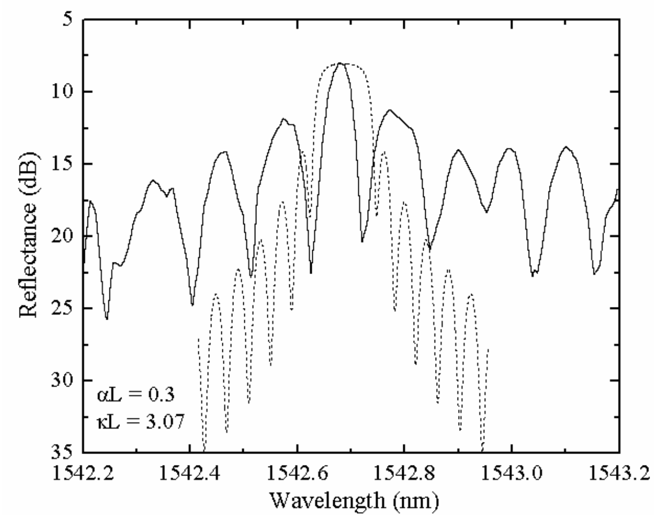

(b)

Figure 5.12 Spectra obtained for a 20 seconds etched grating sample (solid line: experimental, dash line: model). (a) Transmission, and (b) reflection.

The calculated results are generally in a good agreement with the experimental results for the transmittance and reflectance spectra. The side-lobes in the experimental spectra are considerably higher than in the calculated spectra. The higher side lobes could result from non-uniformity in the spatial periodicity of the grating. The listed value of α (~ 0.0246, in Table 5.2) corresponds to an additional loss contribution of 2.7 dB from the 12.5 mm long Si overlay film grating. This value is also in close agreement with the measured insertion loss (~ 5.7 dB) depicted in Figs. 5.10(a) and 5.11(a) for transmission spectra when it is added to the insertion loss of the waveguides without Si film (~3.2 dB), and provides a good match to the peak of reflection spectra in Figs. 5.10(b), 5.11(b), and 5.12(b) when a 3 dB is added to account for the 3-dB fiber coupler. The discrepancy in insertion loss of the transmission spectra for the 20 s etched sample (Fig. 5.12(a)) is likely due to the presence of a damage on the output side of the measurement setup. This sample, however, was not available to repeat the test and correct the observed discrepancy as it had been coated with metal film on its surface for the SEM inspection. The nearly equal bandwidth values between the first two minima relative to the peak in the reflectance and transmittance spectra of each sample, which are observed in both experimental and simulation results, are consistent with a small value of α.

Calculating the spectral width between the first two reflection minima from the expression $\Delta\lambda = (\lambda^2 / n\pi \mathrm{L})\sqrt{(\kappa \mathrm{L})^2 + \pi^2}$ [29] which assumes ideal lossless waveguide grating gives values that are slightly larger than those obtained experimentally, for all

tested samples. This verifies that the presence of loss α affects the value of such a defined spectral width.

C. Polarization Intensity Modulator (PIM)

A series of optical tests of the polarization intensity modulator (PIM) was carried out using the setup in Fig. 5.13. The PIM has been fabricated on the same sample as DBFM and BFPM with identical electrodes and waveguide configuration for proper comparison.

Figure 5.13 Test setup for DC and RF modulation of the polarization intensity modulator (PIM).

A coherent laser beam which has a wavelength of nearly 1543 nm at room temperature passes a fiber polarization controller to set a linear polarization at an angle of $+45^{o}$ relative to the *z*-axis, as indicated in Chapter IV. A fiber butt coupling couples the beam into the waveguide through an optically polished edge. The output optical

signal exiting from the output facet, also optically polished, is collimated by the objective lens, passes the analyzer which has an angle perpendicular to the input polarization, and directed to the photodiode (Newport, Model 981-IR). Voltage is applied to electrodes through a pair of probes for modulation.

At first, tuning DC-voltage was applied to the device. The measured intensity as a function of applied DC-voltage is shown in Fig. 5.14. Using LabVIEW™ and NI-DAQ, the power reading on the power meter is transferred to the computer, and stored as a screen display and a data set.

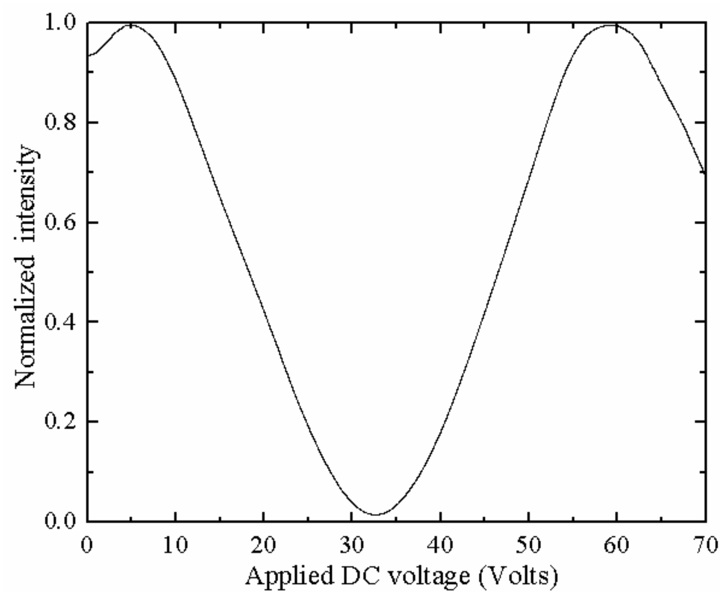

Figure 5.14 DC-voltage response of output optical power of the PIM.

As mentioned earlier, the refractive index change by the application of voltage induces phase modulation in PIM. The analyzer which has an angle perpendicular to the

input polarization converts the phase modulation into intensity modulation. In Figure 5.14, the normalized intensity of PIM is revealed to have a sinusoidal characteristic to the applied DC-voltage, as anticipated from equations (3.9) and (3.10). The voltage required to induce a π-radian phase shift (V_{π}) is measured to be ~27.5 volts. In other words, a minimum DC-voltage of ~27.5 volts is needed to drop maximum output power to minimum, or vice versa in PIM.

A series of low frequency RF voltage modulation tests followed the DC-voltage tuning test. As for a RF modulating voltage source, a function generator (Hewlett Packard, Model 3325B) and a AC power amplifier (Hewlett Packard, Model HP 3325B) were used to provide a modulating voltage. To have deep modulation depth, the laser wavelength was tuned to have the output optical intensity at the quadratic point before the RF voltage is applied. During the modulation, the applied RF voltage to electrodes and the detector signal voltage were traced as a function of time on an oscilloscope. As shown on Figure 5.15 (a), stable traces of output optical signal which depicts modulation with a 1-kHz triangle waveform were observed. By exceeding the allowed voltage limit of peak-to-peak 27.5 volts, the distortion in the signal was observed as shown in Fig. 5.15 (b).

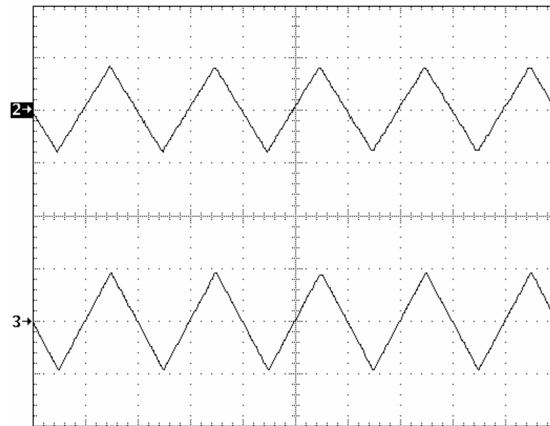

(a)

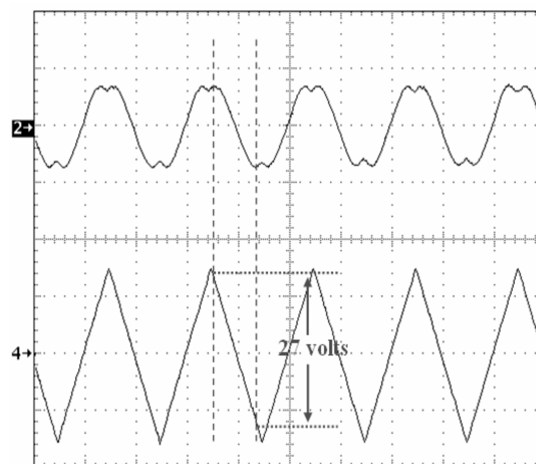

(b)

Figure 5.15 RF polarization intensity modulation of PIM. Upper traces are the optical output and lower traces are the electrical waveform at 1-KHz. (a) Applied peak-to-peak 18 volts (10V/div), and (b) applied peak-to-peak 28.7 volts (10V/div).

The modulation depth is defined by

$$Modulation \quad depth = \frac{Max. \quad power - Min. \quad power}{Max \quad power}. \tag{5.1}$$

The maximum modulation depth of 98.4% and V_π of 27 volts acquired in the RF modulation test are in good agreements with the DC tuning test results.

D. Distributed Bragg Feedback Intensity Modulator (DBFM)

A distributed Bragg feedback intensity modulator (DBFM) as illustrated in Fig. 3.4 was used for the test. The period of the grating is approximately 350 nm and the gap distance between the electrodes is 20 μm.

In order to see the effect of the segment length of the Bragg grating, a couple of broadband transmission spectra measurements using an EDF laser setup (Fig. 5.2) were performed for the sample before and after the formation of the 2-mm segment , shown in Fig. 5.16. By reducing the grating segment length from 14 mm to 2 mm, the insertion loss decreased from 7.1 dB to 6 dB, and the transmission dip changed from 12.75 dB to 12 dB. From this experiment, it seems that a 2 mm of grating segment is enough for more than 90% of reflection efficiency. In both cases, the Bragg wavelengths remained consistent at 1541.238 nm.

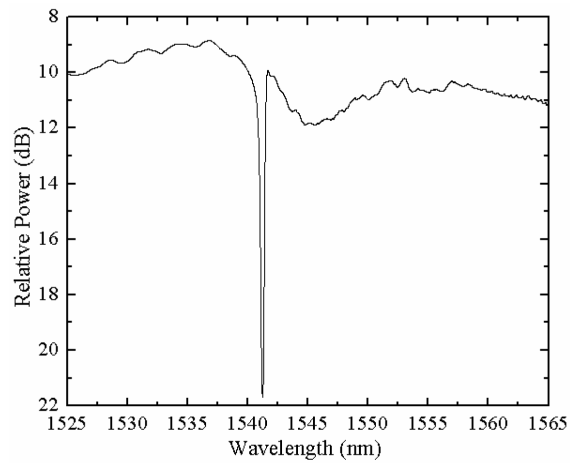

(a)

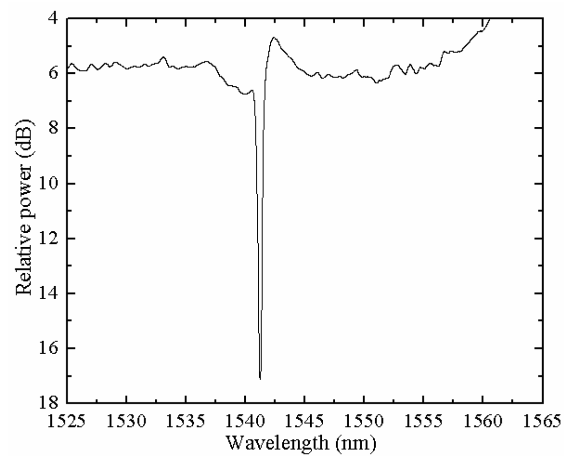

(b)

Figure 5.16 Broadband EDF transmission spectra obtained for 20 seconds etched DBFM device. (a) Before reducing the segment length (12 mm), and (b) after reducing the segment length (2 mm).

Figure 5.17 shows the measured spectral transmission and reflection using the thermal tuning of the DFB laser. Unlike the EDF laser, the temperature tuning of the

DFB laser covers a very short range of the spectrum. To locate the transmission dip in the middle of the DFB laser tuning range, the substrate had to be heated to 29°C using a thermoelectric cooler (TEC) placed underneath the substrate. The transmission spectrum shows one distinct dip at Bragg wavelength (defined by the wavelength which satisfies the Bragg diffraction condition) and a few side-lobes. The Bragg wavelength shown is 1542.36 nm.

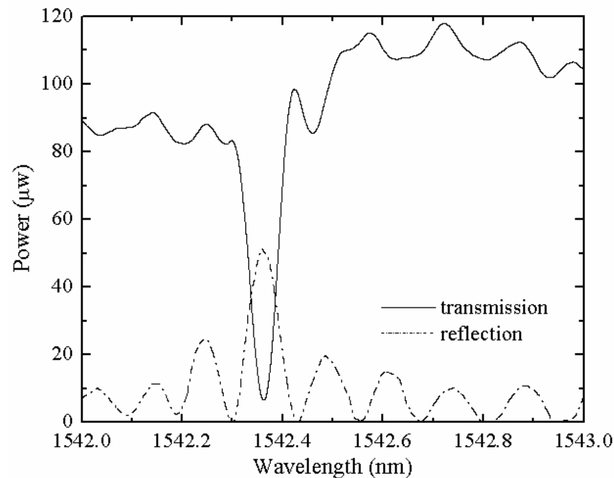

Figure 5.17 Measured narrowband spectra of DBFM for TE input polarization using a thermal tuning of the DBF laser.

Spectrally, the transmission dip of the grating sample is 95%, and spectral width (FWHM) is 0.065 nm which is 0.015 nm wider than that of 14 mm Bragg grating segment. The measured fiber-to-fiber insertion loss for DBFM is 5.5 dB.

For a given change in the effective index which is induced by applied voltage, there is a resulting shift in Bragg wavelength due to the change in the effective index. The PIM changes the phase which results in the polarization change due to the applied voltage. However, the DBFM produces the transmitted power change by the applied voltage. As noted in chapter III, the amount of the Bragg wavelength shift due to the applied voltage can be expressed as

$$\Delta\lambda_{Bragg} = \Lambda \cdot n_{eff}^3 r_{33} \frac{V}{g} \cdot \Gamma \tag{5.2}$$

where Λ is the period of the grating, n_{eff} is the effective index of the waveguide, r_{33} is the electrooptic coefficient (30.8×10^{-12} m/v), V is the applied voltage, g is the electrode separation gap (= 20 μm), and Γ is the electrical-optical field overlap integral. Figure 5.18 shows the measured Bragg wavelength shift as a function of applied DC-voltage.

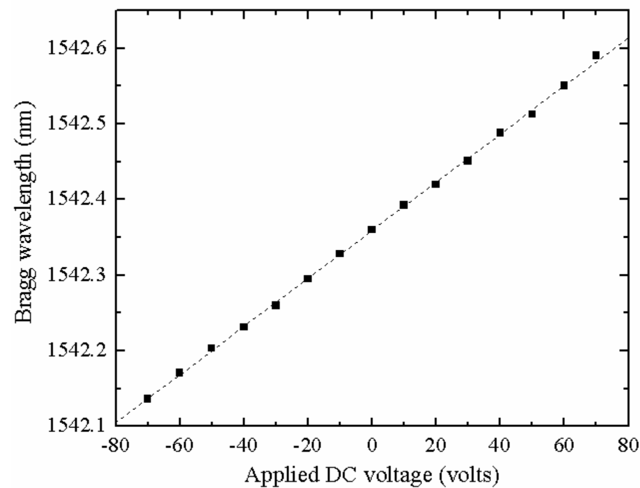

Figure 5.18 Bragg wavelength shift as a function of applied DC-voltage in DBFM.

The Bragg wavelength shift was recorded while sweeping the DC-voltage in the range of -70 to +70 volts. The tuning of the Bragg wavelength was linear with respect to the applied DC-voltage which is in good agreement with the linear electrooptic effect shown in equation (5.2). The dotted line in Figure 5.18 is a linear fit of the measured data in which the slope denotes the amount of the Bragg wavelength shift per unit voltage which is 0.00316 nm/volt. Plugging the approximate values of Λ=350 nm, and n_{eff} =2.14 (for TE polarization) [30], a theoretical expectation value of Bragg wavelength shift per unit voltage is 0.00575 nm/volt when the overlap integral factor Γ is assumed to be unity. The deviation 0.00212 nm/volt of the measurement from the expectation value appears because of the voltage drop across the silicon film and the overlap between the electric and optical fields. It indicates that only 60% of the applied electric field contributes to the effective index change in this DBFM.

Figure 5.19 shows the transmission and reflection spectra of the Bragg wavelength shift by the applied DC-voltage. The applied DC-voltage was swept to have -50, 0, and +50 volts. The narrow band spectrum was plotted as a function of the wavelength at each voltage. At each measurement, the input coupling was slightly adjusted by moving the butt-coupled fiber position to restore the same power level.

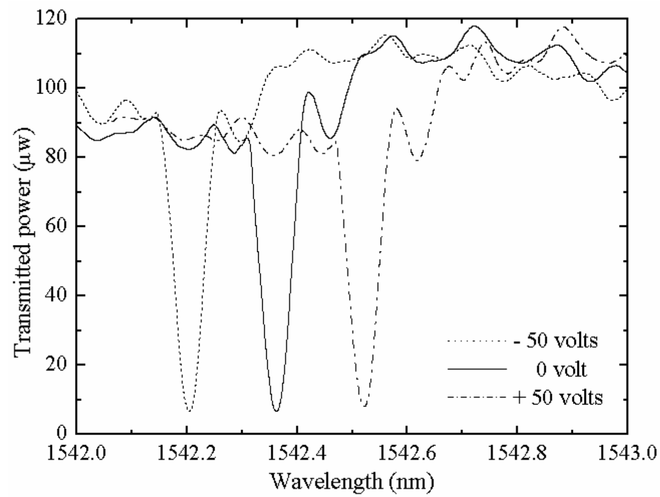

(a)

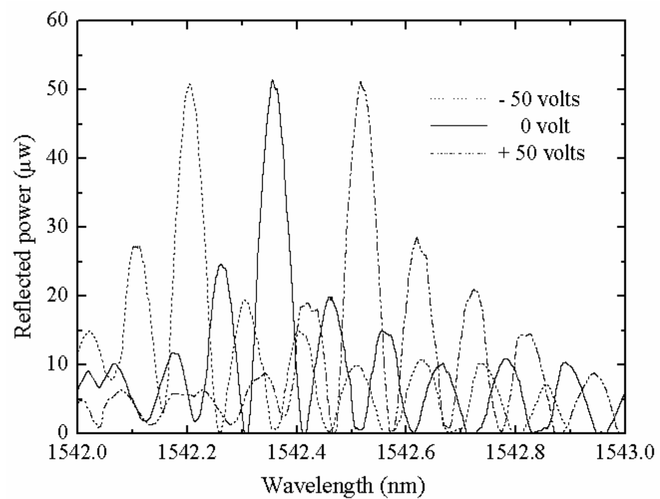

(b)

Figure 5.19 Spectra of Bragg wavelength shift in DBFM by DC-voltage obtained using DFB laser; (a) transmission, and (b) reflection.

DC-voltage tuning tests were conducted to find the switching voltage, which is defined by the voltage required to tune the power from maximum to minimum (or vice

versa); this corresponds to the half wave voltage V_π in the PIM. The transmitted and reflected powers in response to applied DC-voltage are shown in Fig. 5.20. The tests were performed on the setup shown in Fig. 5.5, and the data acquisition was carried out in the same manner as in PIM. As shown in Fig. 5.20, the measured switching voltage from the DC-voltage sweep results is about 16 volts, which is in good agreement with the measured value of Bragg wavelength shift (Fig. 5.19) considering the spectral width and Bragg wavelength shift by unit voltage. The modulation depths of the transmission and reflection are 94% and 98% respectively, which is comparable to that of PIM.

As indicated earlier, the output optical intensity variation of PIM by applied DC-voltage has a sinusoidal nature. To obtain modulation with smaller applied voltage at the same efficiency, the field overlap integral factor should be increased in equation (3.10). However, in the case of DBFM, the drop-off in transmittance (or rise in reflectance) by applied voltage becomes another important factor which is determined by the coupling behavior among modes inside the waveguide with the Bragg grating. Stronger coupling of modes induced by grating as well as an increase the overlap integral factor can generate a sharper cut-off and result in intensity modulation with very small modulating voltage.

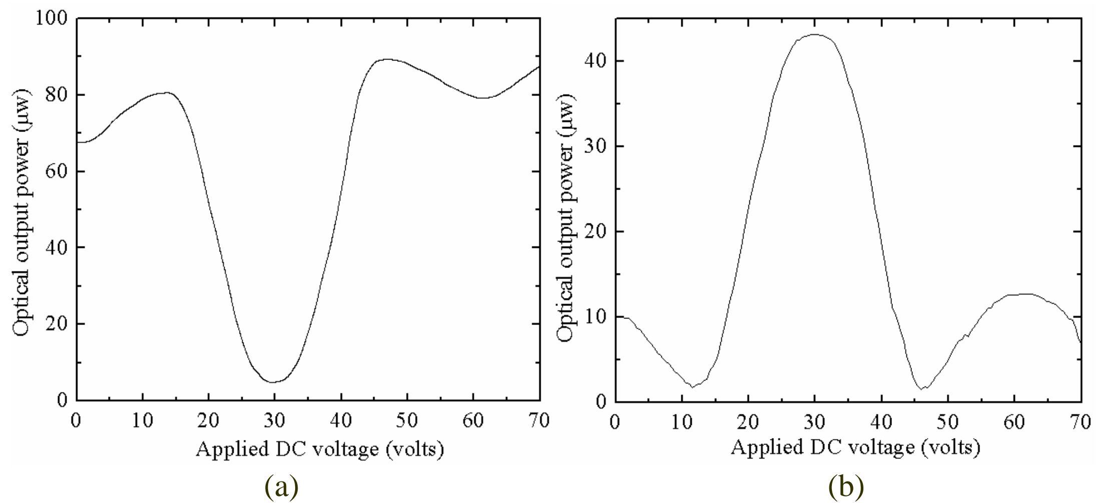

Figure 5.20 DC-voltage tuning response of DBFM; (a) transmitted, and (b) reflected optical output power.

After conducting the DC-voltage tuning tests, a series of RF modulation tests were carried out by adjusting the transmittance (or reflectance) at the middle point between maximum and minimum output power through the laser diode temperature and substrate temperature control. Then an RF voltage signal was applied to the electrodes. The transmission and reflection modulation response to a 1-kHz triangular waveform voltage is depicted in Fig. 5.21.

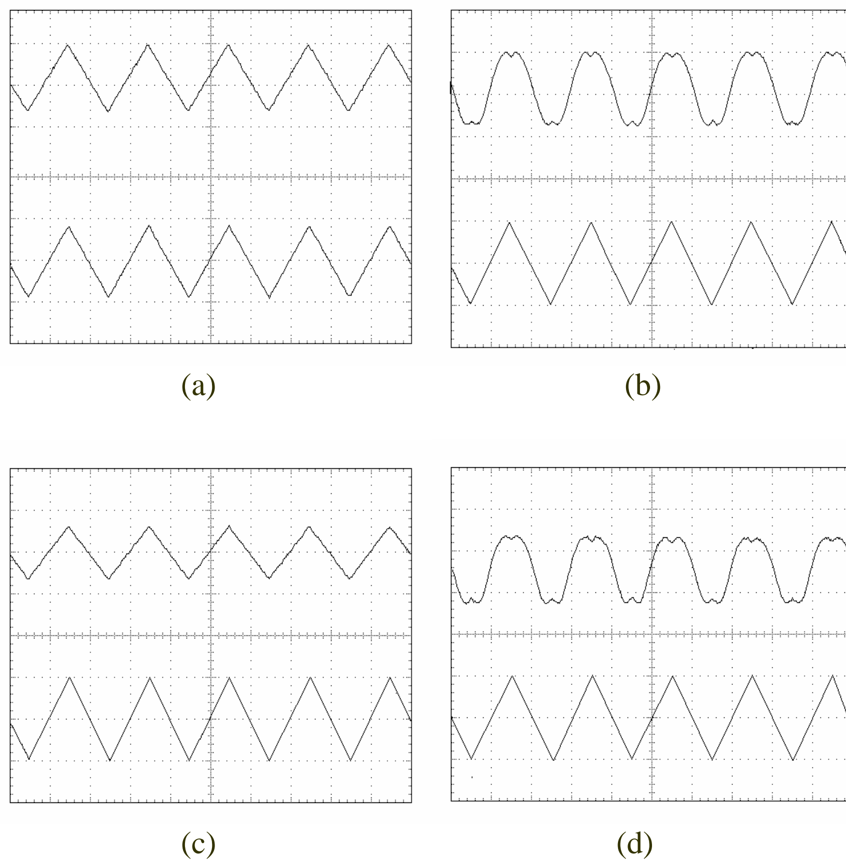

Figure 5.21 RF modulation of DBFM. Upper traces are the optical output and lower traces are the electrical waveform at 1-kHz. (a) Transmission: applied peak-to-peak 8.6 volts (5V/div), (b) transmission: applied peak-to-peak 20 volts (10V/div), (c) reflection: applied peak-to-peak 10 volts (5V/div), and (b) reflection: applied peak-to-peak 20 volts (10V/div).

The switching voltage for the transmitted modulated signal is shown in Fig. 5.22.

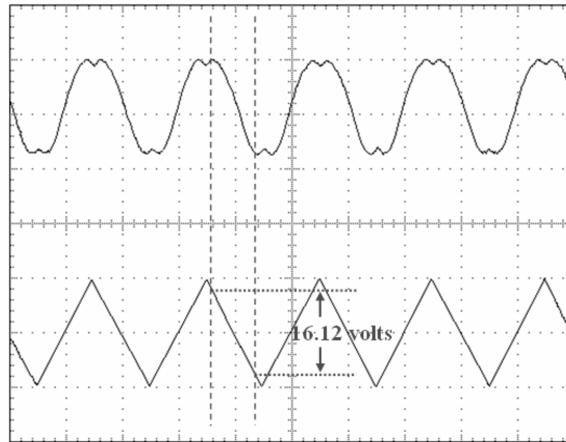

Figure 5.22 Transmission RF modulation of DFBM. Upper trace is the optical output, and lower trace is the electrical waveform at 1-kHz (10V/div).

The switching voltage measured from RF modulation is 16 volts which is identical to DC tuning. The modulation depths are 94% for transmission, and 98% for reflection. Compared with the polarization intensity modulator (PIM) with identical electrodes and waveguide structure without the Bragg grating, the switching voltage in the case of DBFM is reduced by a factor of 1.7 relative to the PIM half-wave voltage (27.5 V). This indicates that the DBFM provides more efficient method for modulation.

E. Bragg Reflector Fabry-Perot Modulator (BFPM)

A Bragg reflector Fabry-Perot modulator (BFPM) as illustrated in Fig. 3.6 was used for testing. As noted earlier, the device is fabricated in the same substrate in order to have identical configurations in waveguide and electrode as those of PIM and DBFM for proper comparison in modulation behavior. In BFPM, each Bragg grating segment acts as a partial reflecting mirror for the specific wavelength which satisfies the Bragg condition, and the pair of Bragg grating segments form a Fabry-Perot cavity. However, due to the reflective nature of the Bragg grating, the cavity length is determined by the efficiency of the Bragg grating with an imaginary mirror located somewhere inside the Bragg grating.

The broadband optical transmission measurements before and after forming a Fabry-Perot cavity are depicted in Fig. 5.23. The appearance of resonance in the spectrum around the Bragg wavelength of ~1541.2 nm due to the formation of the Fabry-Perot structure is noticeable in Fig. 5.23 (b). As the deviation of the wavelength ($\Delta\lambda = \lambda_{Bragg} - \lambda$) from the Bragg wavelength becomes larger, it is clear that the Fabry-Perot interferometer effect dramatically reduces; the reflectivity of the mirror starts to decrease and the two grating segments cease to reflect the light. The maximum transmission dip is 12 dB and the measured fiber-to-fiber insertion loss for the Fabry-Perot Bragg reflector modulator was about 6 dB from the broadband experiments.

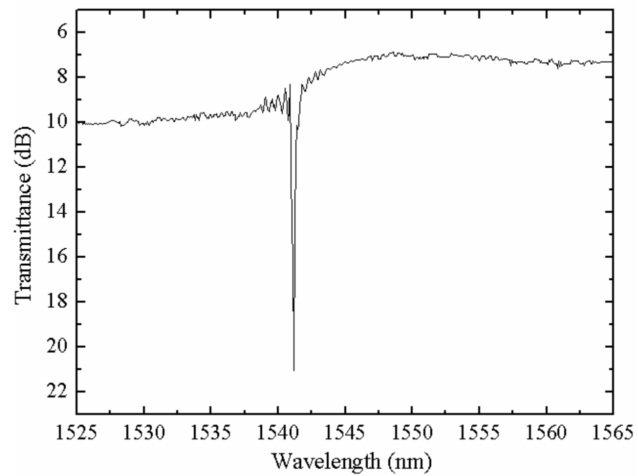

(a)

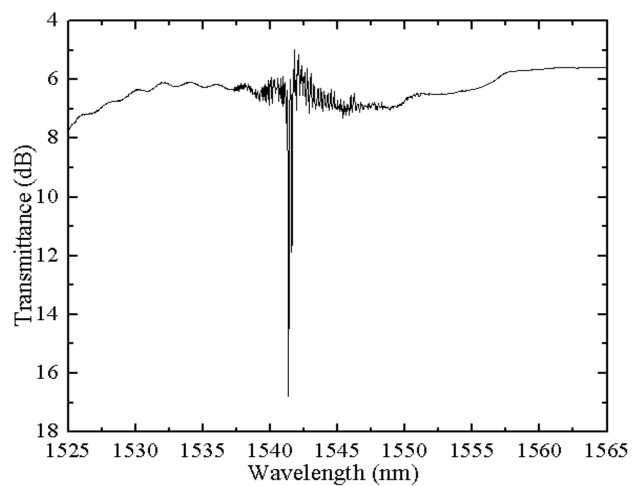

(b)

Figure 5.23 Broadband EDF transmission spectra obtained for a 20 seconds etched BFPM. (a) Before etching the segment length (12 mm), and (b) after producing Fabry-Perot configuration (each segment is 2 mm, and two segments separated by 3 mm).

Narrowband spectral behavior was monitored using the thermal tuning of a DFB laser setup (Fig. 5.5), and the result is shown in Fig. 5.24.

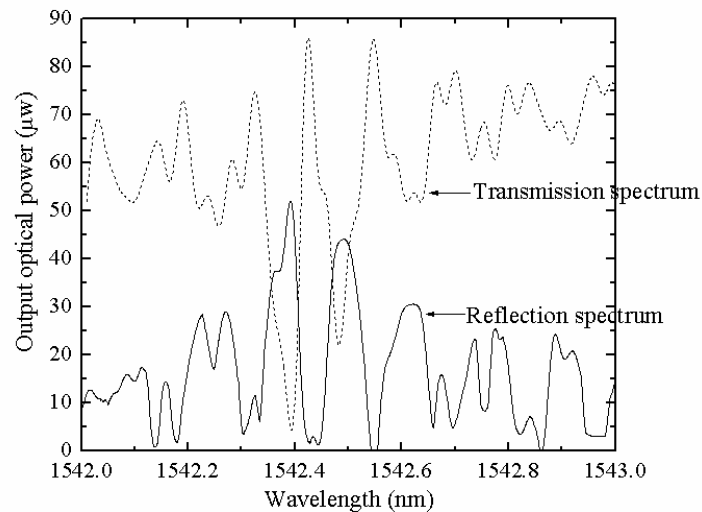

Figure 5.24 Narrowband spectra from BFPM for a TE input polarization using the thermal tuning of a DBF laser.

The Bragg wavelength measured before the formation of a Fabry-Perot cavity was 1542.36 nm. The largest Fabry-Perot effect observed around 1542.4 nm in Fig. 5.24 matches well with the 12-mm long single segment Bragg grating result. Whereas the spectrum from the conventional Fabry-Perot interferometer with film end-face mirrors [25] depends only on the optical phase shift inside the cavity, the result shown in Fig. 5.24 indicates that the spectrum of BFPM relies on the phase shift due to the Fabry-Perot interferometer, as well as reflectivity change caused by the wavelength shift of the Bragg diffraction condition. In the reflection spectrum (Fig. 5.24), numbers of minima are

observed that originate from both primary dip in Fabry-Perot spectrum and the side lobes in the Bragg reflection. A careful inspection was carried out to separate the spectral minima generated by the Fabry-Perot cavity from the minima originated from the Bragg diffraction grating to identify the Fabry-Perot characteristics of the device from the spectrum. As a result, an average free spectral width (FSR) which has a value of 0.128 nm could be obtained. Assuming the maximum Bragg diffraction appears at λ = 1542.36 nm and n_{eff} = 2.14 [30], an approximate effective cavity length (assuming single film mirror replaces the Bragg grating segment) can be evaluated as 4.3 mm, which is reasonable compared to the device structure configuration from equation (2.52). Compared to the spectral width of the first minima in the reflection spectrum of single segment Bragg grating which is $\Delta\lambda_{minima}$ = 0.106 nm, the difference between FSR and $\Delta\lambda_{minima}$ is only 0.022 nm. That explains why only one sharp cut-off from Fabry-Perot spectrum can possibly exist because of the narrow Bragg grating spectral width. Shortening the cavity length by reducing the distance between the grating segments or broadening the Bragg spectral width by generating less gratings, more Fabry-Perot sharp cut-off are expected to be observed around the Bragg wavelength. As noted in Chapter III-D, the sharp cut-off of the spectrum is defined by the finesse of the Fabry-Perot cavity that is a function of the mirror reflectivity. This sharp cut-off in transmission (or reflection) makes it possible to generate modulators of high-sensitivity consuming less modulating voltage. DC-voltage tuning tests were conducted to find the switching voltage (equivalent to V_π of PIM*)*. The transmission and reflection power response of the

device, tested with a DFB laser, as a function of increasing applied DC-voltage are illustrated in Fig. 5.25.

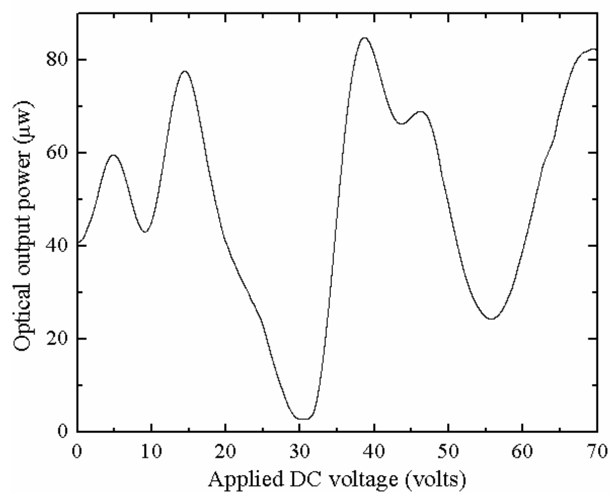

(a)

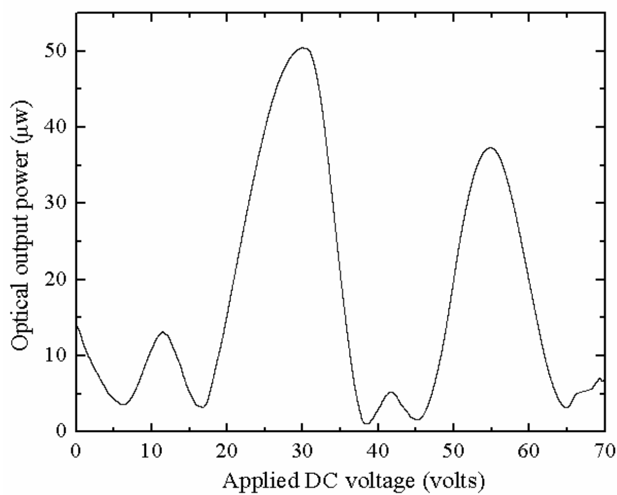

(b)

Figure 5.25 DC-voltage modulation response of BFPM; (a) transmitted power, and (b) reflected power.

As indicated in the DFB measurement spectra, there appeared only one sharp drop, around 33-volts, in optical output power. This sharp drop originates from the Fabry-Perot cavity. However other comparably gradual drops are thought to come from the transition induced by Bragg diffraction. The measured switching voltage from Fig. 5.25 is 7.5 volts which is the smallest among those of PIM and DBFM with identical waveguide and electrode configurations. From equations (2.51) and (2.52), it is expected that the switching voltage can be further reduced by increasing the mirror reflectivity which determines the finesse of the Fabry-Perot cavity. The measured DC tuning modulation depths for transmission and reflection power were both 98 %.

The RF modulation test with a 1-kHz triangular waveform voltage is shown in Fig. 5.26. Before application of the RF voltage to electrodes, the transmittance (or reflectance) was tuned to midway between maximum and minimum through the DFB laser diode temperature adjustments to the emission wavelength at 1542.34 nm.

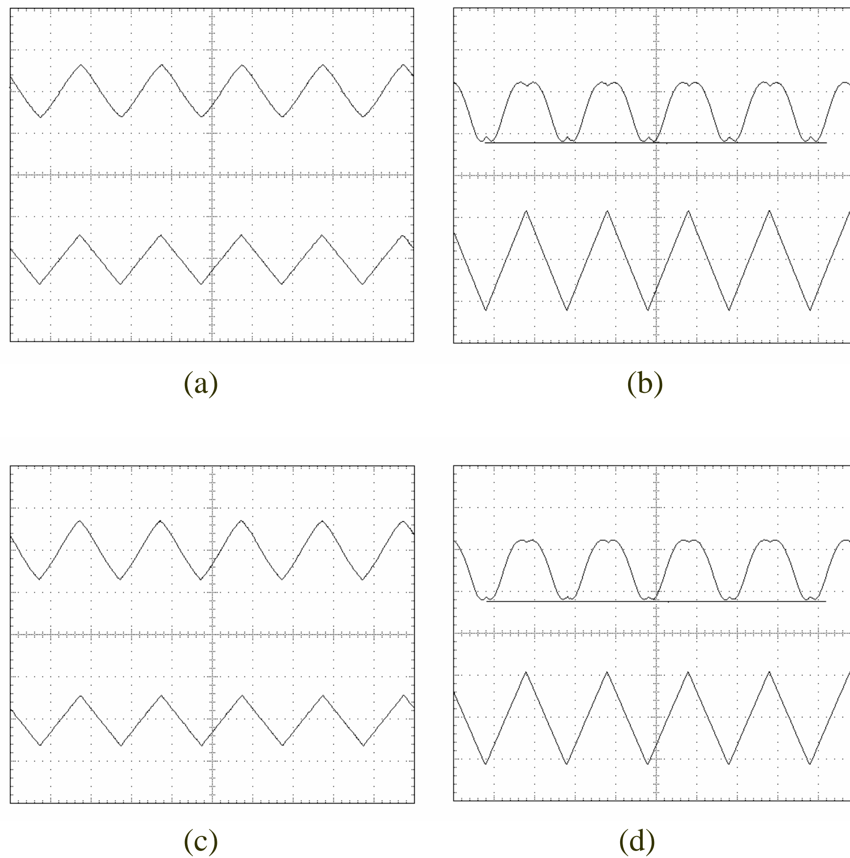

(a) (b)

(c) (d)

Figure 5.26 RF modulation of BFPM. Upper traces are the optical output and lower traces are the electrical waveform at 1-kHz. (a) Transmission: applied peak-to-peak 6 volts (5V/div), (b) transmission: applied peak-to-peak 12 volts (5V/div), (c) reflection: applied peak-to-peak 5.5 volts (5V/div), and (d) reflection: applied peak-to-peak 11 volts (5V/div).

The RF modulation depth was measured to have a value of 98% for both transmission and reflection modulations, which is the same as the DC tuning case. The

switching voltage is determined from the distorted response of the modulator to an applied large amplitude modulation signal, as shown in Fig. 5.27.

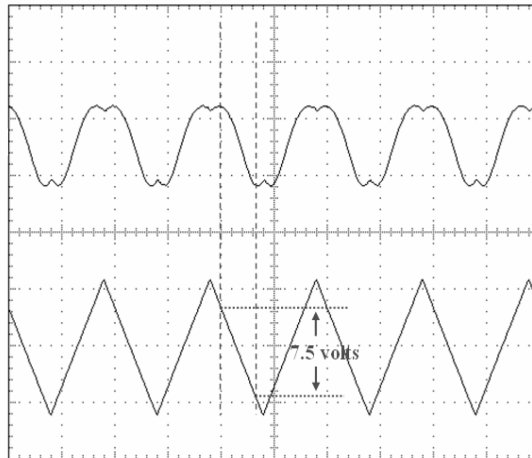

Figure 5.27 Distorted modulation waveform of transmitted power for switching voltage measurement of BFPM. Upper trace is the optical output and lower trace is the electrical waveform at 1-kHz (5V/div).

The measured switching voltage is 7.5 volts which is in a good agreement with the value from the DC-voltage tuning response. Compared to those of the PIM and the DBFM, the switching voltage of the BFPM is 1/3.7 times that of PIM (V_π = 27.5 volts), and 1/2.2 times that of DBFM (switching voltage ~ 16 volts). Considering that those modulators have identical waveguide and electrodes, it is clear that the small switching voltage results from the effect of a Bragg reflector Fabry-Perot cavity. However, the

modulation depth of 98% was very close to that of PIM and DBFM which indicates the BFPM improved the modulation efficiency.

1. Bragg Reflector Fabry-Perot Modulator (BFPM) with Short Electrodes

To investigate the effect of the electrode length on the modulation behavior, another BFPM with a shorter electrode was fabricated. Other parameters such as waveguide and Bragg Fabry-Perot cavity were identical with those of the BFPM with long electrodes. The configuration of the device is illustrated in Fig. 5.28.

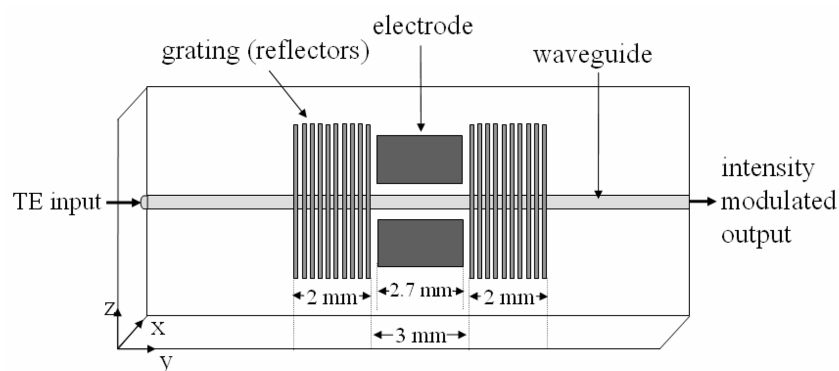

Figure 5.28 Schematic diagram of BFPM with short electrodes.

While the length of electrode in the previous BFPM was 12-mm, it is reduced down to 2.7-mm and located between the Bragg segments in this configuration.

The spectral characteristics of the BFPM with 2.7-mm electrodes are shown in Fig. 5.29**.** Because both the BFPM with long and short electrodes are identical in

waveguide and Fabry-Perot Bragg grating segments, the broadband and narrowband spectra of the BFPM with short electrodes are indistinguishable from that of long electrodes whose spectra are shown in Fig. 5.23 (b) and Fig. 5.24.

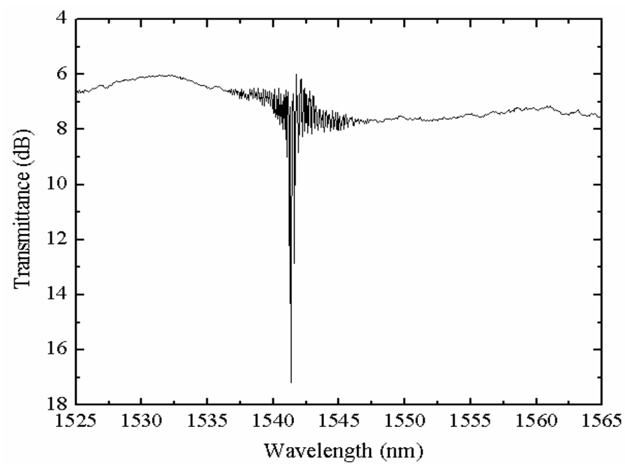

(a)

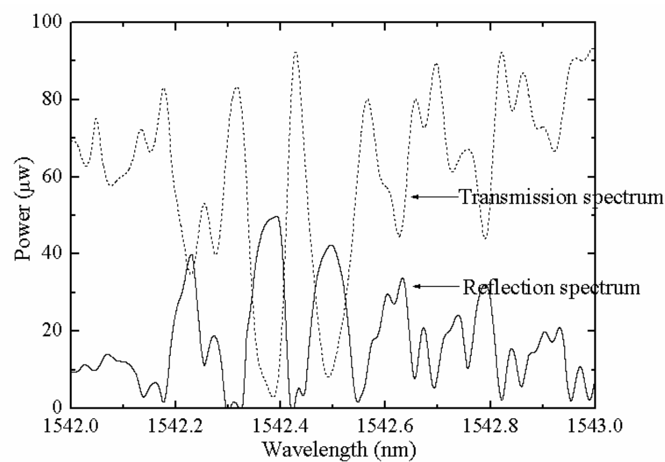

(b)

Figure 5.29 Broadband and narrowband spectra for TE input polarization of BFPM with short electrodes. (a) Broadband spectrum using an EDF, and (b) narrowband spectra using a DFB laser.

However, because the electric field interaction length is short, the transmittance (or reflectance) is modulated primarily by the phase shift factor in equation (3.18) and there is no shift in Bragg wavelength hence reflectivity. This leads to a larger switching voltage value compared to the case of the modulator with a long electrode. To determine the expected half-wave voltage V_π value, the DC-voltage response of the short-electrode BFPM is examined as shown in Fig. 5.30. In both cases of transmission and reflection, the required DC-voltage to switch from maximum to minimum intensity is 27 volts, which as anticipated is much larger than that of BFMP with longer electrode.

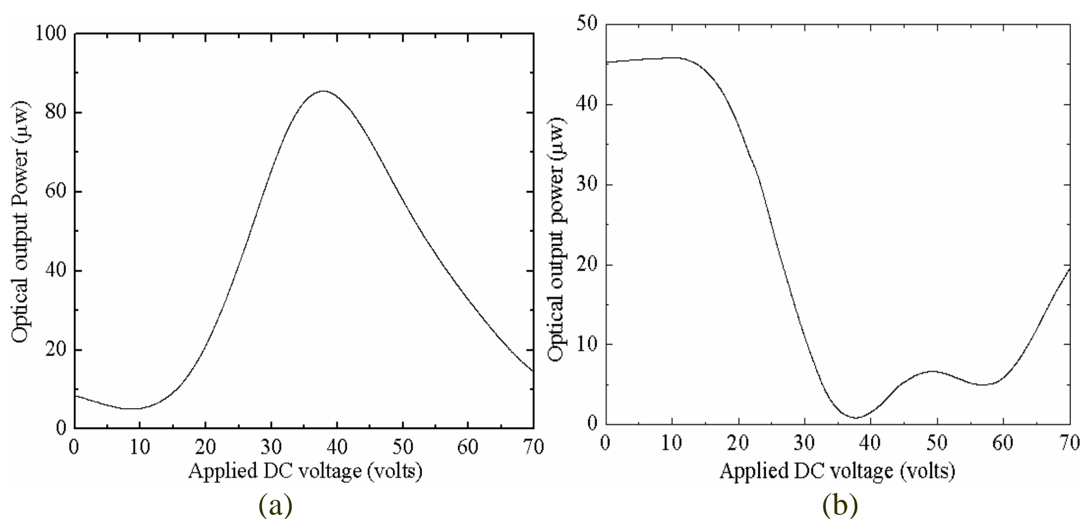

Figure 5.30 DC-voltage modulation response of BFPM with short electrodes; (a) transmitted power, and (b) reflected power.

The RF modulation test with a 1-kHz triangular waveform voltage (Fig. 5.31) confirms this result.

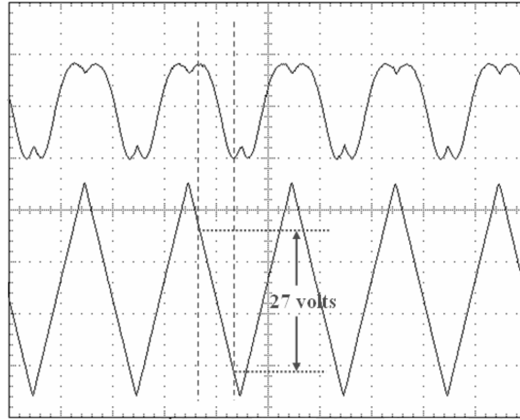

Figure 5.31 Distorted modulation waveform for transmitted power for BFPM with short electrodes. Upper trace is the optical output and lower trance is the electrical waveform at 1-kHz (10V/div).

F. Frequency Response of the Modulators

To predict the frequency response of the modulators, the lumped equivalent circuit model was used [31]. The equivalent RLC circuit model of the lumped modulator used in this prediction is shown in Fig. 5.32.

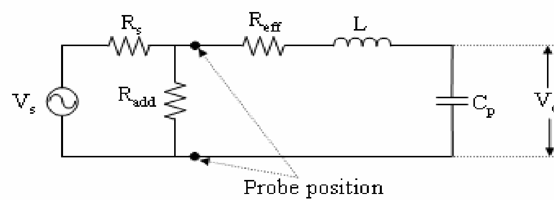

Figure 5.32 Equivalent circuit model of a lumped electrode modulator.

In Figure 5.32, V_s is the source RF voltage, R_s is the source impedance, R_{add} is an added resistance at the probe terminal, R_{eff} is the effective resistance of the electrode, L is the inductance of the electrodes, C_p is the parallel capacitance of the electrodes, and V_o is the voltage across the electrodes. R_{add} was designed to provide a certain amount of input impedance matching for the purpose of increasing the bandwidth of the output. Before the simulation, the circuit element values were measured. The measurement was performed by using a precision LCR meter (Hewlett Packard, model: 4284A). The measured values of the resistance per unit length r and the capacitance C_p were 2 Ω/mm with a 12 mm long electrode and 35 pF, respectively. And the inductance of the electrode is assumed to be very small with the probes and was neglected. The value of R_{eff} can be determined from the measured electrode resistance per unit length, $r = 2$ Ω/mm, with the distributed electrode being $R_{eff} = 2rL_e / 3 = 16\ \Omega$.

Theoretically, the magnitude of the voltage ratio across the parallel capacitor which represents the electrodes in the Figure 5.32 can be expressed as [31]

$$\frac{V_o(f)}{V_o(f=0)} = \frac{\left(1/\omega C_p\right)}{\left[\left(R_{add}/2 + R_{eff}\right)^2 + \left(\omega L - 1/\omega C_p^2\right)\right]^{1/2}}. \tag{5.3}$$

The frequency response of the electrical power across the capacitor in dB is

$$\mathrm{P_{elect}} = 20 \log\left[\mathrm{V_o(f) / V(f=0)}\right] \tag{5.4}$$

where $V_o(f)$ is the voltage across the capacitor at a certain frequency and the $V(f = 0)$ is the voltage across the capacitor at very low frequency. For the calculation of P_{elect}, the Multisim 8™ computer program was used. The relationship among the bandwidth, the

electrical power across the electrode, and the value of the additional resistance was simulated as shown in Fig. 5.33.

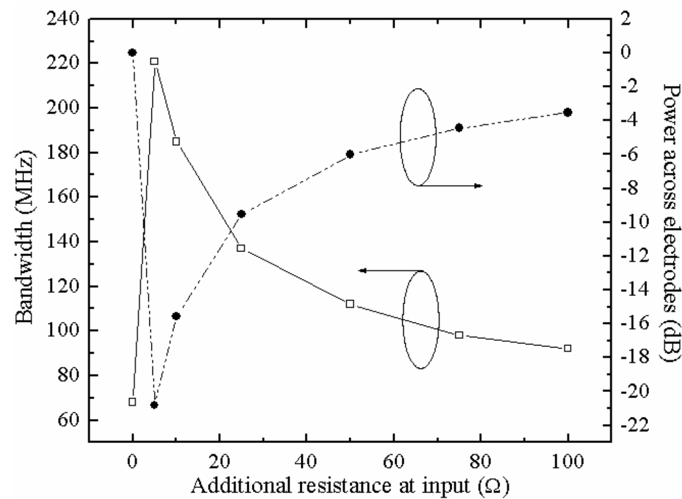

Figure 5.33 The simulation result of the effect on the bandwidth and the electrical power across the electrodes by varying the added resistance.

The simulation result indicates that the electrical power across the electrodes should be sacrificed if the electrical bandwidth of the circuit is to be increased. In order to increase the bandwidth of the circuit with a reasonable delivered electrical power drop across the electrode, the additional resistance value was set to 50 Ω in the experiments. To confirm the effect of the additional resistor on the bandwidth of circuit, a series of modulation tests using the PIM were carried out. Because the optical output power is of interest for the modulator use, the frequency responses of the output optical power of PIM were measured to evaluate the effect of additional resistance on the bandwidth of a

real device. To monitor the response, the amplitudes of a modulated sinusoidal voltage waveform on an oscilloscope and a RF spectrum analyzer were recorded at each frequency. For modulating voltage source, a signal generator (PTS, Model 160) was used. Due to the voltage drop with the frequency ramp and the voltage limit of the signal generator, a RF power amplifier (EIN, Model 3252A) was attached to amplify the modulating voltage at high frequency. A circuit for the power reduction was attached to the RF power amplifier because it supports a fixed amplification of 50 dB (see Appendix 17) of which the high power might burn the electrode. For the optical output power detection, an APD detector (Fujitsu, model FPD13P12JX) with a 3-dB bandwidth of 1 GHz was used. The test result of the modulation frequency response of the optical output power for PIM is shown in Fig. 5.34**.**

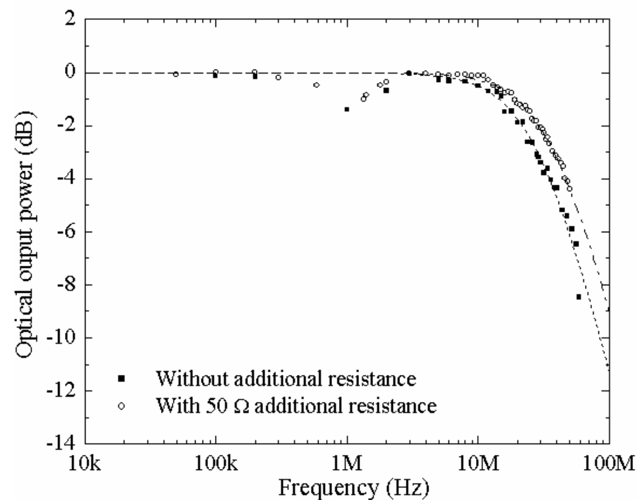

Figure 5.34 Frequency response of the optical power of PIM with and without the 50 Ω additional resistor at the terminal of the probe.

The measured values of the optical 3-dB power bandwidth for 0 Ω and 50 Ω of an additional resistor are ~28 MHz and ~38 MHz, respectively. As expected in simulation results, a 50 Ω additional resistor at the terminal of the probe had proven to increase the 3-dB bandwidth of output optical power.

In practice, the electrical power at the receiver is of interest. A circuit diagram of a photodetector unit is depicted in Fig. 5.35 [32].

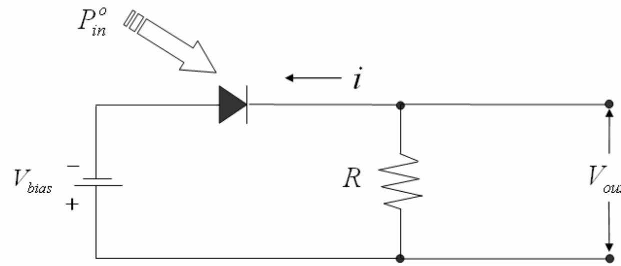

Figure 5.35 Schematic diagram of a photodetector equivalent circuit.

The amount of current generated is proportional to the incident power,

$$i = \rho \cdot P_{in}^{o} \qquad (5.5)$$

where P_{in}^{o} is the incident optical power, and ρ is the responisivity of the photodetector. The output voltage ($V_{out} = i \times R$) which is linearly proportional to the incident optical power is measured at the oscilloscope as a function of frequency response. Because the electrical power of the receiver is proportional to the square of current, the 3-dB frequency of the electrical power of the receiver is defined by $1/\sqrt{2}$ of the voltage

response at zero frequency. Figure 5.36 depicts the frequency response of the PIM, the distributed feedback Bragg intensity modulator (DBFM), and the Bragg reflector Fabry-Perot modulator (BFPM).

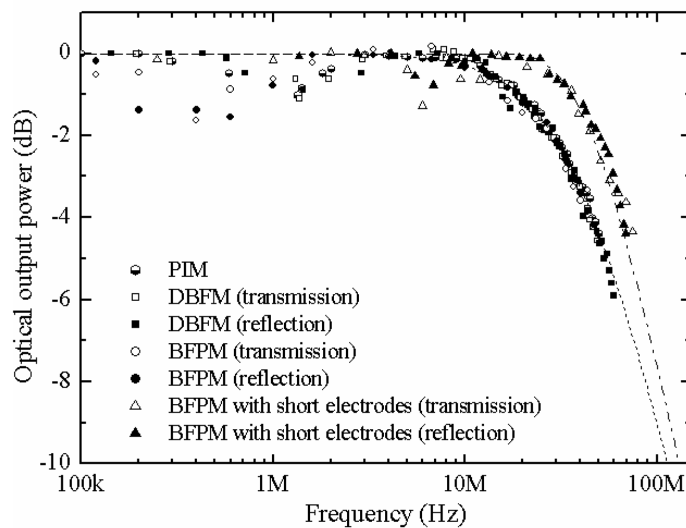

Figure 5.36 Frequency responses of the optical output power of the modulators.

All of the frequency responses of the modulators with same electrode lengths showed similar test results where the 3-dB electrical power frequency falls below 30 MHz. In the case of short electrodes, the 3-dB frequency is 42 MHz. As clearly seen in the results, the 3-dB electrical frequency for the optical output intensity is restricted by limitations in the RLC circuit bandwidth which is proportional to the inverse of RC [22] (Chap. 9, pp. 222-246). The fact that the modulator which has a shorter electrode has smaller RC value than the others explains its higher bandwidth.

In most of the practical optical modulators, the modulation signal is operated in high frequency to utilize the wide frequency bandwidth in the optical communication system. For higher bandwidth, the RLC circuit-bandwidth limitation and transit time limitation in the waveguide should be overcome. A traveling waveguide and a slow-waveguide modulator are methods to overcome such restrictions [33, 4]. By introducing a transmission line concept and velocity matching between light wave and electrical modulating wave, the bandwidth can be dramatically increased.

G. Modulation Sensitivity of the Modulators

The slope of I_{pp} / I_o as a function of V_m / V_π is an indicator of the modulation sensitivity. To compare the modulation sensitivities among different types of modulators, the output optical intensity with a small modulating voltage was examined for the PIM, the DBFM and the BFPM, and shown in Fig. 5.37. For the DBFM and the BFPM, a transmission optical modulation was used for the measurement. Initially, the transmissions of the devices were tuned to move the transmittance to midway between maximum and minimum; then 1-kHz of RF voltage is applied. Switching voltage values used for the PIM, the DBFM and the BFPM are 27.5, 16 and 7.6 volts, respectively, as obtained from the DC and RF voltage modulation tests.

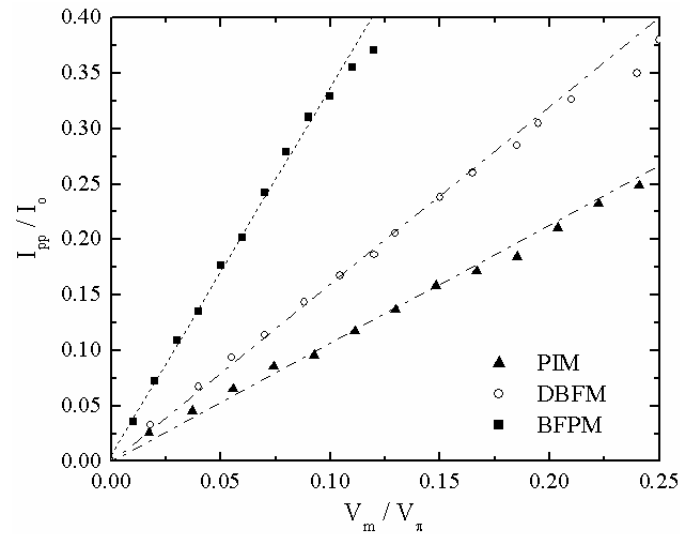

Figure 5.37 Normalized peak-to-peak output intensity as a function of normalized applied modulation voltage.

The slopes in Figure 5.37 can be taken as an indicator of the modulator sensitivity, respectively. The BFPM and the DBFM have 3 and 1.5 times higher slope than PIM. Theoretically, the slope of the PIM is fixed to have the value of π; however, the slopes of the DBFM and the BFPM can be further increased by increasing the Bragg grating reflectivity. The results show that the DBFM and the BFPM are promising as highly sensitive modulators compared to conventional modulators.

CHAPTER VI

CONCLUSIONS

Channel waveguides were fabricated in $LiNbO_3$ by Ti diffusion and a series of microelectronic processes. Parameters such as Ti film thickness and width, diffusion time and temperature were adjusted to produce single mode channel waveguides for both TE and TM polarizations.

Amorphous silicon film was deposited on the surface of $LiNbO_3$ and used to produce gratings. To make the grating pattern in the silicon overlay, a photoresist grating was generated on the surface of the silicon film using a holographic exposure technique with a 459 nm line from an argon-ion laser. The photoresist and exposure setup were optimized for 350 nm period of high resolution photoresist pattern generation. The delineated photoresist pattern was used as a mask to etch spatially periodic corrugations in the Si film. Si film thickness of 105 nm was used to produce the gratings.

With a 105-nm-thick Si overlay and 93 nm deep gratings that were etched for 20 s by reactive ion etching in inductively coupled plasma (RIE-ICP), a relative broadband transmittance spectrum with > 20 dB dip for TE input polarization from a waveguide was obtained. The spectrum had a 3-dB bandwidth of ~ 0.05 nm. The combination of transmission drop and 3-dB spectral width is the deepest and smallest reported for Bragg reflection gratings integrated on $LiNbO_3$.

Using the finite difference method, the Bragg grating spectra in which a loss factor is included was modeled. The calculated results are generally in good agreement

with the experimental results. This model indicates that the presence of loss affects the value of spectral width.

Three types of modulators- a polarization intensity modulator (PIM), a distributed Bragg feedback intensity modulator (DBFM), and a Bragg reflector Fabry-Perot modulator (BFPM) were designed, fabricated and characterized. Identical waveguide and electrode configuration were used for proper comparison.

At a 1-kHz triangular waveform voltage modulation tests, the DBFM and BFPM revealed switching voltages 1/1.7 and 1/3.7 times that of PIM which has a measured value of ~27.5 volts. The modulation depths in all modulators were in the range of 98% ~ 99%. The reduction in switching voltage results from the inherent characteristic of Bragg grating reflectors which shows a sharp cut-off in transmittance. By forming a Fabry-Perot structure, the cut-off becomes even sharper.

Frequency response tests of the modulators revealed similar electrical bandwidth of 28 MHz with 50 Ω shunt resistor at the terminal of probes. Modulation tests using a short electrode BFPM showed larger bandwidth (42 MHz) which confirms the RC limiting effect.

Modulation sensitivity tests with a small modulating RF voltage amplitude were performed on PIM, DBFM, and BFPM devices. The sensitivity to the applied voltage was found to be proportional to the sharpness of transitions in each modulator response and confirmed that the integration of Bragg reflectors on a waveguide is a promising method for making efficient modulators.

CHAPTER VII

SUGGESTIONS FOR FUTURE WORK

The important parameters for optical modulators are low operating voltage and broad operation bandwidth. As shown in this dissertation, Bragg reflectors provide an effective method to reduce the operating voltage when integrated with a modulator. However, the broad operation bandwidth couldn't be realized because of the RC limitation [22]. A traveling-waveguide electrode structure can overcome this problem. The objective of a traveling-wave electrode is to make the electrode behave as a transmission line with impedance matching to the source and the cable which feeds the modulating voltage signal [33]. In addition, the bandwidth may be further increased if the traveling waveguide is used in combination with Bragg gratings, in a slow-wave optical propagation configuration [4].

REFERENCES

[1] F. Koyama and K. Iga, “Frequency chirping in external modulators,” *J. Lightwave Technol.*, vol. 6, pp. 87-93, January 1988.

[2] A. Yariv, *Optical Electronics in Modern Communications*, 5th ed. New York: Oxford University Press, 1997.

[3] N. Shaw, W. J. Stewart, J. Heaton, and D. R. Wight, “Optical slow-wave resonant modulation in electro-optic GaAs/AlGaAs modulators,” *Electron. Lett.*, vol. 35, pp. 1557-1558, September 1999.

[4] H.F. Taylor, “Enhanced electrooptic modulation efficiency utilizing slow-wave optical propagation,” *J. Lightwave Technol.*, vol. 17, pp. 1875-1883, October 1999.

[5] J. B. Khurgin, J. U. Kang, and Y. J. Ding, “Ultrabroad-bandwidth electro-optic modulator based on a cascaded Bragg grating,” *Opt. Lett.*, vol. 25, pp. 70-72, January 2000.

[6] A. Melloni, F. Morichetti, and M. Martinelli, “Linear and nonlinear pulse propagation in coupled resonator slow-wave optical structures,” *Opt. Quantum Electron.*, vol. 35, pp. 365-379, March-April 2003.

[7] S. Hinz, D. Sandel, M. Yoshida-Dierolf, V. Mirvoda, R. Noé, G. Feise, H. Herrmann, R. Ricken, W. Sohler, H. Suche, F. Wehrmann, and R. Wessel, “Polarisation mode dispersion compensation for 6ps, 40 Gbit/s pulses using distributed equaliser in $LiNbO_3$,” *Electron. Lett.*, vol. 35, pp. 1185-1186, July 1999.

[8] B.K. Das, R. Ricken, and W. Sohler, "Integrated optical distributed feedback laser with Ti:Fe:Er:$LiNbO_3$ waveguide," *Appl. Phys. Lett.*, vol. 82, pp. 1515-1517, March 2003.

[9] S. Fouchet, F.R. Ladan, F. Huet, A. Carenco, M. Carre, and Y. Gao, "Ti-implanted Bragg reflectors on $LiNbO_3$:Ti stripe waveguides," *Appl. Phys. Lett.*, vol. 58, pp. 1518-1520, April 1991.

[10] H. Feng, R.F. Tavlykaev, and R.V. Ramaswamy, "Record-high reflectance in narrowband low-loss Bragg reflectors with Si-on-$LiNbO_3$ waveguides," *Electron. Lett.*, vol 35, pp. 1636-1637, September 1999.

[11] B. Wu, P.L. Chu, H. Hu, and Z. Xiong, "UV-induced surface-relief gratings on $LiNbO_3$ channel waveguides," *IEEE J. Quantum Electron.*, vol, 35, pp. 1369-1373, October 1999.

[12] Y. Sidorin and A. Cheng, "Integration of Bragg gratings on $LiNbO_3$ channel waveguides using laser ablation," *Electron. Lett.*, vol. 37, pp. 312-314, March 2001.

[13] B.-E. Benkelfat, R. Ferrière, B. Wacogne, and P. Mollier, "Technological implementation of Bragg grating reflectors in Ti:$LiNbO_3$ waveguides by proton exchange," *IEEE Photonics Technol. Lett.*, vol. 14, pp. 1430-1433, October 2002.

[14] S. Pissadakis, L. Reekie, M.N. Zervas, and J.S. Wilkinson, "Grating in indium oxide film overlayers on ion-exchanged waveguides by excimer laser micromachining," *Appl. Phys. Lett.*, vol. 78, pp. 694-696, February 2001.

[15] R.F. Carson and T.E. Batchman, “Multimode phenomena in semiconductor-clad dielectric optical waveguide structure,” *Appl. Opt.*, vol. 29, pp. 2769-2780, June 1990.

[16] G.M. McWright, T.E. Batchman, and M.S. Stanziano, “Measurement and analysis of periodic coupling in silicon-clad planar waveguides,” *IEEE J. Quantum Eelectron.*, vol. QE-18, pp. 1765-1771, October 1982.

[17] J. Kim, G. Li, and K.A Winick, “Design and fabrication of a glass waveguide optical add-drop multiplexer by use of an amorphous-silicon overlay distributed Bragg reflector,” *Appl. Opt.*, vol. 43, pp. 671-677, January 2004.

[18] A. Yariv and P. Yeh, *Optical Waves in Crystals*. New York: John Wiley & Sons, 1984.

[19] J.C. An, Y. Cho, and Y. Matsuo, “Electrooptic-distributed Bragg-reflection modulators for integrated optics,” *IEEE J. Quantum Electron.*, vol. QE-13, no.4, pp. 206-208, April 1977.

[20] R. G. Hunsperger, *Integrated Optics*, 4th edition. Berlin: Springer, 1995.

[21] H. Nishihara, M. Haruna, and T. Suhara, *Optical Integrated Circuits*, New York: McGraw-Hill, 1989.

[22] A. Yariv, *Introduction to Optical Electronics*, New York; Holt, Rinehart and Winston, 1971.

[23] P. E. Green, Jr., *Fiber Optic Networks,* Englewood Cliffs, NJ: Prentice Hall, 1993.

[24] M. Born and E. Wolf, *Principles of Optics*, 6th ed., New York: Pergamon, 1980.

[25] T. Suzuki, J. M. Marx, V. P. Swenson, and O. Eknoyan, "Optical waveguide Fabry-Perot modulators in $LiNbO_3$," *Appl. Optics*, vol. 33, no. 6, pp.1044-1046, February 1994.

[26] Z. Tang, "Study of utilizing static photoelastic effect in intergrated optical devices," Ph.D. Dissertation, Texas A&M University, College Station, 1994.

[27] J. L. Jackel, V. Ramaswamy, and S. P. Lyman, "Elimination of out-diffused surface guiding in titanium-diffused $LiNbO_3$," *Appl. Phys. Lett*., vol. 38, pp. 509-511, April 1981.

[28] E. L. Wooten, K. M. Kissa, A. Yi-Yan,. E. J. Murphy, D. A. Lafaw, P. F. Hallemeier, D. Maack, D. V. Attanasio, D. J. Fritz, G. J. McBrien, and D. E. Bossi, "A review of lithium niobate modulators for fiber-optic communications systems," *IEEE J. Select. Topics in Quantum Electron.*, vol. 6, no.1, pp. 69-82, Jan./Feb. 2000.

[29] B. E. Benkelfat, R. Ferrière, B. Wacogne, and P. Mollier, "Technological implementation of Bragg grating reflectors in Ti:$LiNbO_3$ waveguides by proton exchange," *IEEE Photonics Technol. Lett*., vol. 14, pp. 1430-1433, October 2002.

[30] D. F. Nelson and R. M. Mikulyak, "Refractive indices of congruently melting lithium niobate," *J. Appl. Phys.,* vol. 45, no. 8, pp. 3688-3689, August 1974.

[31] O. Eknoyan, C. H. Bulmer, R. P. Moeller, W. K. Burns, and K. H. Levin, "Guided-wave electro-optic modulator in Ti:$LiNbO_3$ at λ=2.6 μm," *J. Appl. Phys.,* vol. 59, no. 8, pp. 2993-2995, April 1986.

[32] J. C. Palais, *Fiber Optic Communications*, 4th edition, Englewood Cliffs, NJ: Prentice Hall, 1998.

[33] R. C. Alferness, “Guided-wave devices for optical communication,” *IEEE J. Quantum Electron*., vol. QE-17, no. 6, pp. 946-958, August 1981.

APPENDIX 1

CUTTING SUBSTRATES WITH DICING SAW

1. Turn on the vacuum pump and the air flow knob.

2. Turn on the cctv.

3. Remove the plastic house of blade and measure the resistance between the blade and the spindle. The resistance should be less than 1 or 2 kΩ. After the measurement, restore the plastic house.

4. Turn on the power of the dicing saw.

5. Push the program button and check parameters.

   1) Program 300 is used (use the program call if not already there).
   2) Card describes parameters.
   3) Mode is always 30.
   4) Use slow speed (0.127 mm/s) for safety issue.
   5) Use 25000 rpm.
   6) Height = 0.089 mm and thickness = 1.2 mm (add 0.2 mm to substrate thickness).
   7) Dimension is the desired cutting length.

6. Turn off the program, and push the clear button.

7. Clean the chuck with a methanol and a q-tip.

8. Turn on the spindle.

9. Zero the chuck.

10. Lock the wafer onto platform.

11. Press the align button and align the sample with a cross hair on the microscope.

12. After aligning, push the clear button and modify the desired length to be cut.

13. Press the single cut button.

14. After finishing the cutting,

    1) Push the spindle off button.

    2) Push the reset button.

    3) Push the wafer release button.

15. Remove the sample from the spindle.

16. Turn off the spindle.

17. Zero the chuck.

18. Turn off the machine in reverse order of the procedure 1-4.

APPENDIX 2

SUBSTRATE CLEANING PROCEDURE

1. Gently brush with a Q-tip using soapy water.
2. Rinse thoroughly with D.I. water.
3. Sonicate in acetone for 10 minutes.
4. Rinse thoroughly with methanol.
5. Sonicate in methanol for 10 minutes.
6. Rinse thoroughly with D.I. water.
7. Sonicate in soap water for 10 minutes.
8. Rinse thoroughly with D.I. water.
9. Sonicate in D.I. water for 10 minutes.
10. Blow dry with N_2.

APPENDIX 3

DC SPUTTERING PROCESS

1. Turn on the main power of the system.
2. Open the nitrogen tank.
3. Vent the chamber.
4. Open the bell jar.
5. Load the samples and close the bell jar
6. Turn on the chamber-roughing switch.
7. Wait until the roughing pressure drops below 50 μHg.
8. Close the roughing valve and open the high vacuum valve.
9. Turn off the mechanical pump.
10. Turn on the ionization gauge and degas it for 5~10 min.
11. Wait untill the pressure drops to $4\sim6*10^{-6}$ torr, then turn off the ionization gauge.
12. Open the Ar gas tank and flow the Ar gas (140 sccm).
13. Close the high vacuum valve to adjust the system vacuum to 20 μHg.
14. Turn on and increase the voltage to generate the plasma (~ 3200 volts).
15. Presputter as desired.
16. Rotate the sample holder to place the sample under the plasma.
17. When finished, turn the high voltage knob all the way down and turn off the switch.
18. Cool down for 30 min while Ar gas is flowing.
19. Close the gas valve and the high vacuum valve.

20. Vent the systmem and take out the sample.

21. Follow “roughing” and “high vacuum” steps to pump out the system.

22. Close the high vacuum valve and turn off the power.

APPENDIX 4

PHOTOLITHOGRAPHY PROCESS

Positive process.

1. Dehydrate the substrate in the oven at 135ºC for 5 minutes.

2. Spin coat the photoresist for 30 seconds at 5,000 rpm.

3. Soft bake the sample;

   1) Clariant AZ5214: 2 minutes at 100ºC,

   2) Shipley S1805: 1 minute at 99°C.

4. Expose;

   1) Clariant AZ5214: 60 mW·s/cm^2 in U.V. light,

   2) Shipley S1805: for 4 minutes with a power of 0.165 watt in argon laser.

5. Develop;

   1) Clariant AZ5214: Shipley MF312:H_2O mixture (1:1.2 by volume ratio),

   2) Shipley S1805: Shipley MF320:H_2O mixture (1:2 by volume ratio).

6. Thoroughly rinse the sample in DIW and gently blow the substrate with Nitrogen.

Image reversal process.

1. Dehydrate the substrate in the oven at 135ºC for 10 minutes.

2. Spin coat the AZ5214 photoresist for 30 seconds at 5,000 rpm.

3. Soft bake the substrate at 96 ºC for 1 minute.

4. Expose the sample to U.V. light (21.3 mW·s/cm^2) with mask without filter.

5. Post bake the sample at 106 ºC for 2 minutes.

6. Flood-expose the sample to U.V. light (21.3 mW/cm^2 with filter for 2 minutes).

7. Develop the sample with the MF312:H_2O mixture (1:1.2 by volume ratio).

8. Thoroughly rinse the sample in DIW and gently blow the substrate with Nitrogen.

APPENDIX 5

O_2 PLASMA ASHING PROCESS

1. Turn on the power supply and the vacuum pump.
2. Set the temperature of the chamber to 135ºC, and wait until it reaches to the temperature.
3. Vent the chamber and load the substrate.
4. Pump out the chamber and O_2 line to a pressure of 50 µHg.
5. When the temperature reaches 130ºC, flow O_2 gas and adjust the chamber pressure to 500 µ*Hg*.
6. Set the forward RF power to 100 W while keeping the reflected RF power below 5 W.
7. Count the time.
8. When finish, vent the system and take out the substrate.
9. Set the temperature setting to 20ºC.
10. Turn off the vacuum pump and the power supply.

APPENDIX 6

REACTIVE ION ETCHING (RIE) PROCESS

1. Turn on the main power.

2. Turn on the mechanical pump.

3. Turn on the cooling water system.

4. Vent the chamber

5. Load a sample.

6. Close the chamber.

7. Open the roughing valve.

8. Wait until the pressure reaches below 7,000 μHg.

9. Close the roughing valve, and open the high vacuum valve.

10. Turn on the blower RIE switch.

7. Wait until the pressure drops to 20 μHg or below.

8. Flow Ar, CHF_3, and He into the chamber by the rate of 3 sccm for Ar, 7.5 sccm for He, and 30 sccm for CHF_3.

9. Change the flow switch to auto, and wait until the pressure indicator shows 70 and the gas flow stabilizes.

10. Turn on the RF power, adjust the forward power to 350 mW and reflected power below 0 mW.

11. Start etching and timing.

12. When the etching finishes, turn off the RF power, and close all gas valves and switches. Wait for 2 minutes.

13. Close the high vacuum valve, turn off the baratron and the blower, the vent chamber, and take out the substrates.

APPENDIX 7

HIGH TEMPERATURE TITANIUM DIFFUSION PROCESS

1. Load well cleaned substrates onto an alumina (Al_2O_3) holder, and put the holder in the center of big alumina tube.

2. Locate the alumina tube to the center (flat temperature region) of furnace tube.

3. Seal the furnace tube with a cap at front and connect the bubbler.

4. Turn on the compressed air and adjust the airflow.

5. Adjust the settings for a desired temperature.

6. Wait until the airflow stabilizes at 1 bubble/second, and then turn on the control switch.

7. Wait until the current meter stabilizes, then turn on the element switch.

8. Wait until the furnace temperature reaches to a desired temperature.

9. When the current meter starts to swing on/off, begin counting the diffusion time.

10. Keep the bubbling rate at 1 bubble/second throughout the process.

11. After completion of the diffusion, turn off the element and control switches.

12. After 3-4 hours, the temperature should drop below 200ºC, then close the gas and remove the quartz cap at the front.

13. After the furnace temperature drops to room temperature, take out the substrate.

APPENDIX 8

WAVEGUIDE EDGE POLISHING PROCESS

1. Apply one small drop of a U.V. cure epoxy (Norland optical adhesive, P/N 8101) to the substrate waveguide surface.

2. Place another substrate on top of the first one, so that both waveguide surfaces face each other.

3. Secure mount to the polishing fixture.

4. Expose the pair to U.V. light for 10 minutes at each end in order to cure the epoxy.

5. Mix 0.5 teaspoon of polishing grit with lapping oil and spread mixture evenly over the lapping plate.

6. Polish at a speed of 6 rpm for 10-15 minutes.

7. Unfasten mounting fixture from the polishing jig and clean with isopropyl alcohol.

8. Mix 3 μm diamond polishing grit with water, soap, and suspendix following the mixing formula.

9. Pour the solution into the polishing wheel and the tray.

10. Put the polishing jig onto the plate.

11. Turn on the pump to circulate the slurry mixture.

12. Polish for about 50-60 minutes with the speed of 18 rpm.

13. Clean the substrate and inspect the edges under the microscope before moving on.

14. Clean all the equipments thoroughly.

15. Repeat the fine polishing procedure with 0.3 μm diamond polishing grit for 45 minutes at 16 rpm.

16. Clean and inspect the edge quality under the microscope. If needed, repeat polishing.

17. Clean all the equipment thoroughly.

18. Soak the substrate into MF312 until they separate.

19. Clean the substrate with methanol and water.

20. Inspect the edge quality and cleanness under the microscope prior to an optical testing.

APPENDIX 9

ELECTRON BEAM DEPOSITION PROCEDURE

1. Mount the substrate on the plate.

2. Test the thickness monitor. If working properly, the light should blink twice.

3. Vent the system with a nitrogen gas.

4. Load samples and target materials in a carbon boat into the system.

5. Turn on the mechanical pump and open the roughing valve.

6. Pump the system until the pressure reaches below 70 μHg.

7. Close the roughing valve and open the high vacuum valve.

8. Pump the system until the pressure reaches below $5x10^{-6}$ Torr.

9. Setup the thickness monitor.

10. Turn on the cooling water system.

11. Plug-in the key.

12. Turn on the main power, and wait for the system to start.

13. Press the high-voltage-on button, and wait for the relay to turn on.

14. If the current shows, turn off the high voltage immediately. A short circuit is presented.

15. Turn on the scanner.

16. Wait for the filament to warm up.

17. Increase the current gradually, and adjust the light spot position to start the deposition.

18. After finishing the deposition, turn down the current and voltage. Plug off the key.

19. Turn off the thickness monitor.

20. Wait for 5 minutes, and turn off the power supply.

21. Wait for 15 minutes, close the cooling water for crystal, and turn off the crystal cooler.

22. Wait for 45 minutes, and close other cooling waters under the front panel.

23. Turn off the hi-vacuum switch.

24. Vent the system, and take out samples.

25. Once everything has been removed from the chamber, rough the chamber slightly.

26. Turn off the main control.

APPENDIX 10

ARGON LASER OPERATION PROCEDURE

Argon-ion laser: Spectra-Physics, Model BeamLok™

1. Open cooling water line on the wall.

2. Turn on "*System III*" water chiller.

3. Flip up the wall power box switch.

4. Turn on the Z-lok power box.

5. Bring the laser key.

6. Turn on the laser control panel by rotating the laser key; Wait until the relay clicks.

7. Start with "*CUR*" (current) mode.

8. Increase the current to the maximum (58.8~58.9 amps).

9. Warm it up for an hour with the maximum current setting of 58.9 amperes.

10. After the power exceeds 0.1 watt, the beam-lok cross display will have green light on it.

11. Turn on the etalon lock.

12. Switch the "*CUR*" mode to "*PWR*" mode.

13. Adjust the laser power by rotating the "*PWR*" knob.

14. If the "*PWR*" once set, it's no need to adjust it every time.

15. After fixing the laser power, leave it more than 20 min to stabilize it.

16. The laser is ready to be operated.

17. To turn off the laser, switch the "*PWR*" mode into "*CUR*" mode for the next use; the current reaches maximum.

18. Rotate the key to shut down the system.

20. Turn off the "*Etalon Lock*".

21. Wait for 5 min with the water cooler is still on.

22. Turn off the power of "*System III*" water chiller.

23. Shut off four yellow water levers behind the "*System III*" water chiller.

24. Close the two middle yellow valves on the wall.

25. Open the two top yellow valves on the wall to circulate the water.

APPENDIX 11

TWO BEAM INTERFERENCE PRINCIPLE

Interference is defined by a coherent summation of wave amplitudes. The interference of two plane waves with identical wavelengths is illustrated in Fig. A.1.

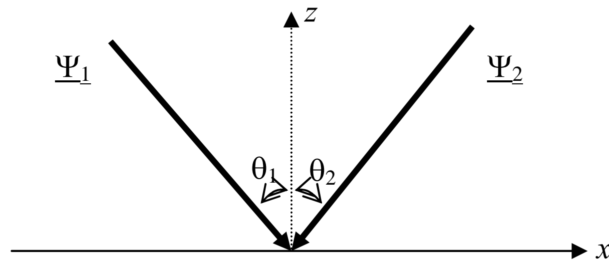

Figure A.1 Schematic diagram of the two plane waves incident on a plane containing *x*-axis.

The electric field of each wave can be expressed in forms of

$$\underline{\Psi_1} = \underline{A_1} \cdot e^{-j(\omega t - \underline{\beta_1} \cdot \underline{r})}, \tag{A.1}$$

and

$$\underline{\Psi_2} = \underline{A_2} \cdot e^{-j(\omega t - \underline{\beta_2} \cdot \underline{r})} \tag{A.2}$$

where A_i is the field amplitude, ω is the radian frequency, β (=2πn/λ) is the propagation constant, and $\underline{r}$ is the directional vector of Ψ_i. $\underline{\beta} \cdot \underline{r}$ can be expressed by

$$\underline{\beta} \cdot \underline{r} = \beta(\sin\theta_i \cdot x + \cos\theta_i \cdot z) \tag{A.3}$$

where θ_i is the angle from the normal to *x*-plane. The intensity can be expressed as

$$P = \left(\underline{\Psi_1} + \underline{\Psi_2}\right) \cdot \left(\underline{\Psi_1} + \underline{\Psi_2}\right)^* \tag{A.4}$$

The photoresist is located at $z = 0$. The intensity at $z = 0$ is expressed as

$$\begin{aligned} P &= \left(A_1 e^{j\beta x \cdot \sin\theta_1} + A_2 e^{j\beta x \cdot \sin\theta_2}\right) \cdot \left(A_1 e^{j\beta x \cdot \sin\theta_1} + A_2 e^{j\beta x \cdot \sin\theta_2}\right)^* \\ &= A_1^{\ 2} + A_2^{\ 2} + 2A_1 A_2 \cdot \cos(x\beta \sin\theta_1 - x\beta \sin\theta_2). \end{aligned} \tag{A.5}$$

As shown in equation (A.5), a sinusoidal intensity variation appears on *x*-plane by the coherent interference of the plane waves (Fig. A.2).

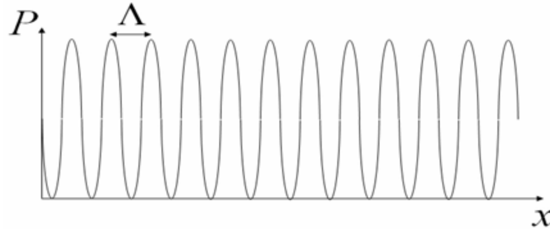

Figure A.2 Schematic diagram of the intensity variation on the *x*-plane by two beam interference.

By setting $x\beta \sin\theta_1 - x\beta \sin\theta_2 = 2\pi$, the spatial period Λ of the light intensity variation is found as

$$\Lambda = \frac{\lambda}{n(\sin\theta_1 - \sin\theta_2)}. \tag{A.6}$$

As a result, this period becomes the period of photoresist pattern after the development.

APPENDIX 12

SEM PHOTOGRAPH OF GRATING PATTERN WITH THICK SILICON FILM

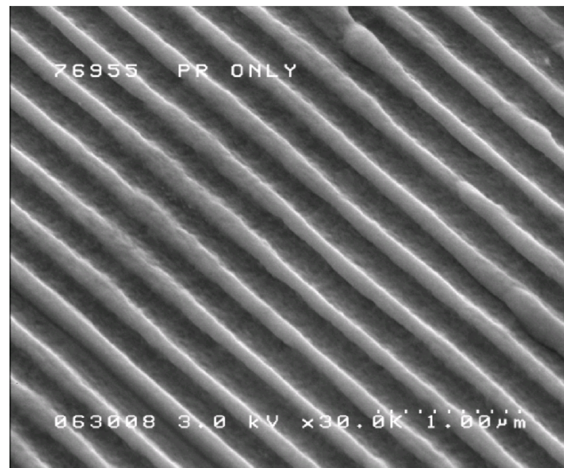

(a)

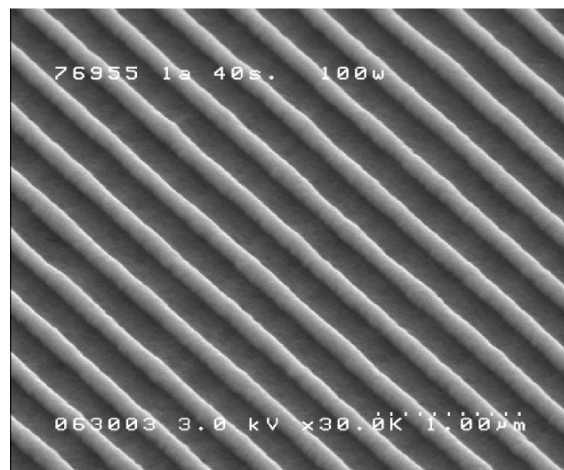

(b)

Figure A.3 SEM photographs of (a) photoresist grating pattern, and (b) silicon grating pattern with the silicon film thickness of 1400 Å for 40 seconds at 100 W in RIE-ICP.

APPENDIX 13

MANUFACTURER (NTT) SUPPLIED SPECIFICATION OF DFB LASER

The DFB laser diode (NTT, Model NLK1556STG-BX) is in a butterfly-type 14 pin package with a thermo-electric cooler (TEC). Single mode fiber pigtailed from the laser has a SC/PC connector at the other end.

Table A.1 Manufacturer supplied electrical/optical characteristics of the DFB laser at $T_{sub}=25^oC$.

Parameter	Symbol	Condition	Min.	Typ.	Max.	Units
Forward Voltage	V_F	$I_F=30mA$		1.2	1.6	V
Threshold current	$I_{(TH)}$	CW		10	20	mA
Fiber output power	Φ_o	CW, $I_F=110mA$	20			mW
Peak wavelength	λ_p	CW, $\Phi_o=20mW$		1543		nm
Spectral linewidth	$\Delta\nu$	CW, $\Phi_o=20mW$		2		MHz
Side mode suppression ratio	SMS	CW, $\Phi_o=20mW$	35			dB
Dark current (PD)	$I_{(0)}$	CW, $V_{DR}=5V$			100	nA
Thermistor resistance	R	$T_{sub}=25^oC$		10		kΩ
Isolation	I_s	$T_{sub}=25^oC$		30		dB

APPENDIX 14

LabVIEW™ PROGRAMMING FOR GPIB AND DATA ACQUISITION (NI-DAQ™)

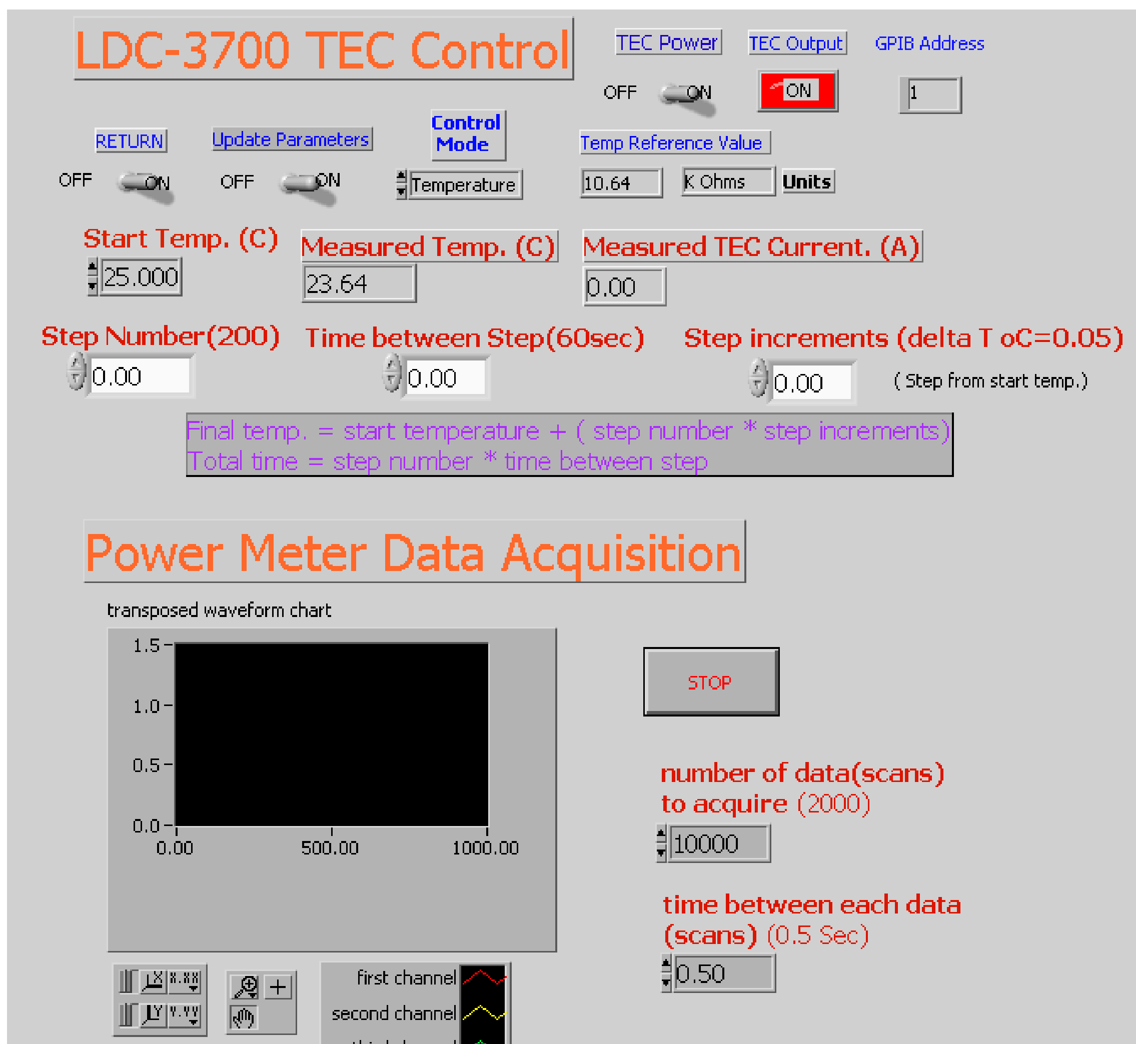

Figure A.4 The LabVIEW™ front panel for the GPIB control and the data acquisition.

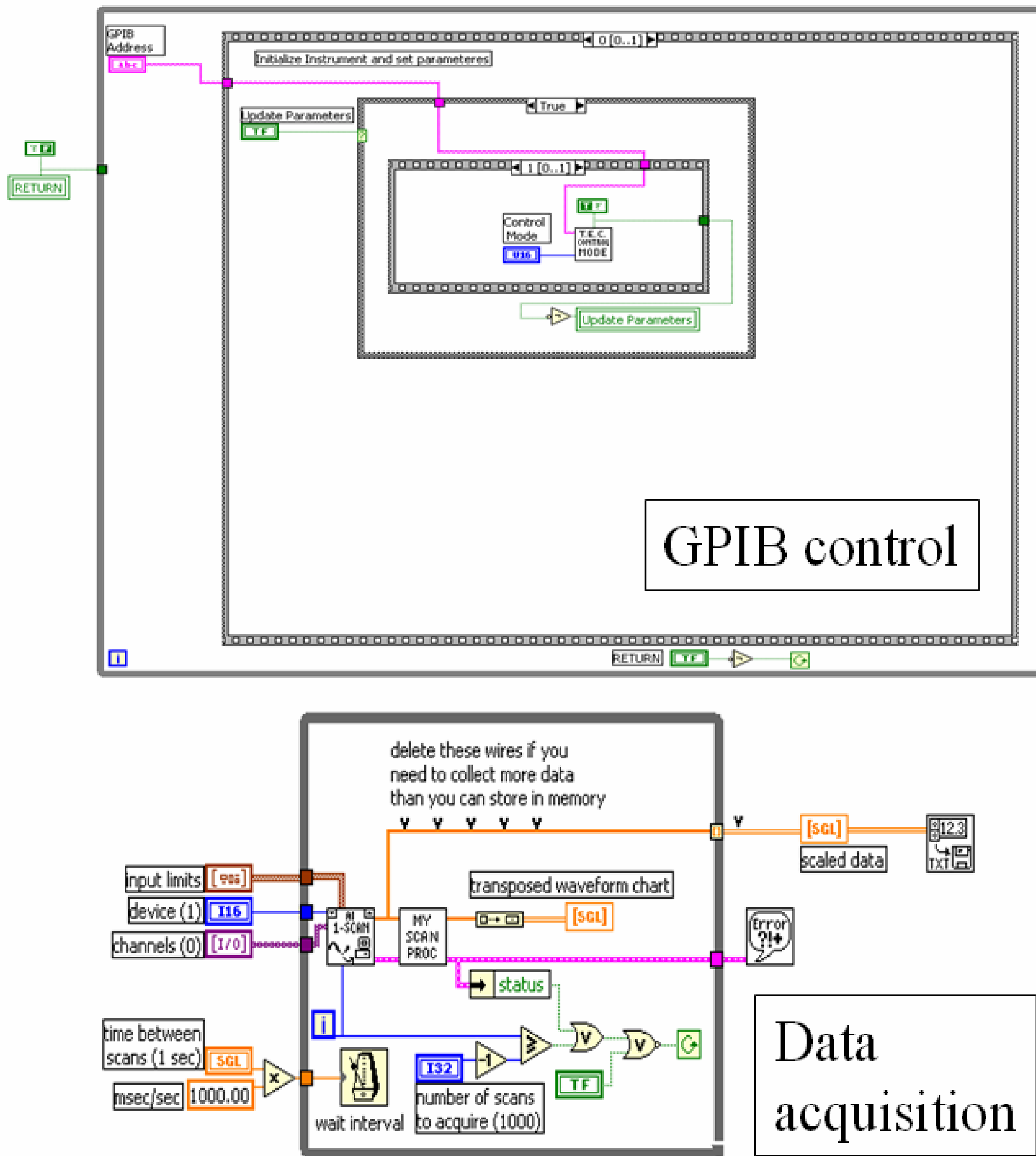

Figure A.5 The LabVIEW™ block diagram for the GPIB control and the data acquisition.

APPENDIX 15

DFB LASER CHRACTERISTICS

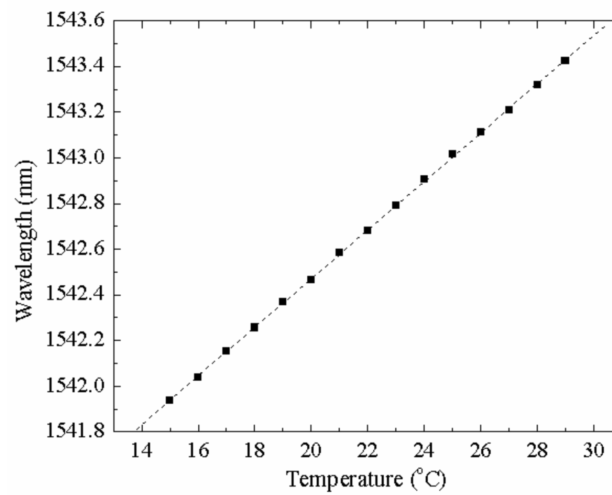

Figure A.6 Temperature tuning of the DFB laser wavelength.

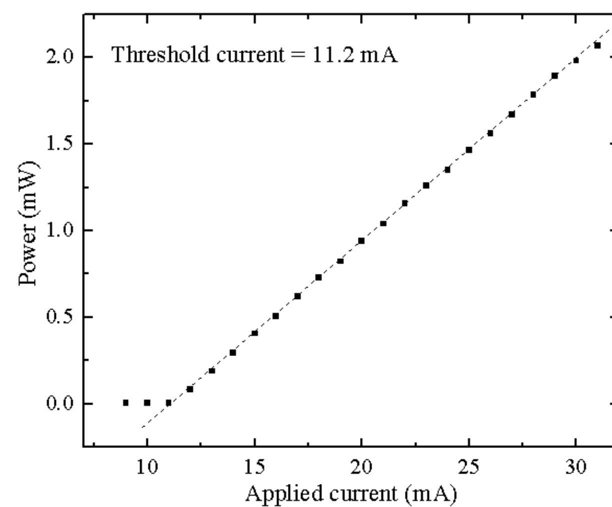

Figure A.7 Applied current vs. output power of the DFB laser.

APPENDIX 16

C++ FINITE DIFFERENCE METHOD SIMULATION PROGRAMMING

```
# include <fstream.h> // gratingkim2 created 1/17/05

#include <math.h>  //

# include<iomanip.h>  // contradirectional coupling

void main ()  //modified 1/17/05

{

double  aar[1000],aai[1000],bbr[1000],bbi[1000];

double al,kap,dz,z,alL,kapL,f,delzmax,delz,A,B,pi,lam,n,L;

double cs,sn,ar,ai,br,bi,dar,dai,dbr,dbi,ddelz,T,R,dlam,Clam;

int i,j,k,N,nz,ndel;

pi=3.1415927;

n=2.2;

L=1.25e-2;

lam = 1.53e-6;

Clam=4*pi*n*L/(lam*lam);


ofstream g1("h:\\desktop\\grating simulation\\saved\\g1.txt");

f=1;

delz=0;

while (f>0)
```

```
{
cout<<"Read alL  kapL  nz ndel delzmax \n";
cin>>alL>>kapL>>nz>>ndel>>delzmax;
dz=1./nz;
ddelz=2.*delzmax/ndel;
delz=-delzmax;
for(k=1;k<=ndel;k++)
{

aar[nz]=1;
aai[nz]=0;
bbr[nz]=0;
bbi[nz]=0;
for(i=1;i<=nz;i++)
{
j=nz-i;
z=(j+.5)*dz;
cs=cos(delz*z);
sn=sin(delz*z);
ar=aar[j+1];
ai=aai[j+1];
br=bbr[j+1];
```

```
bi=bbi[j+1];
dar=kapL*(br*cs-bi*sn)-alL*ar;
dar=dar*dz;
aar[j]=aar[j+1]-dar;
        dai=kapL*(bi*cs+br*sn)-alL*ai;
dai=dai*dz;
aai[j]=aai[j+1]-dai;
        dbr=kapL*(ar*cs+ai*sn)+alL*br;
dbr=dbr*dz;
bbr[j]=bbr[j+1]-dbr;
        dbi=kapL*(ai*cs-ar*sn)+alL*bi;
dbi=dbi*dz;
bbi[j]=bbi[j+1]-dbi;
}
         A = aar[0]*aar[0]+aai[0]*aai[0];
     B = bbr[0]*bbr[0]+bbi[0]*bbi[0];
 T=10*log10(1./A);
 if(B>.0000001)
 R=10*log10(B/A);
 else
 R=0;
 dlam=delz/Clam;
```

```
 dlam=dlam*1.e9;
       g1<<delz<<"\t"<<dlam<<"\t"<<T<<"\t"<<R<<"\t"<<endl;
       cout<<delz<<"\t"<<T<<"\t"<<R<<endl;
   delz=delz+ddelz;
}
cout<<"Read f  > 0 continue\n";
cin>>f;
}
}
```

APPENDIX 17

A CIRCUIT DIAGRAM FOR RF POWER REDUCTION

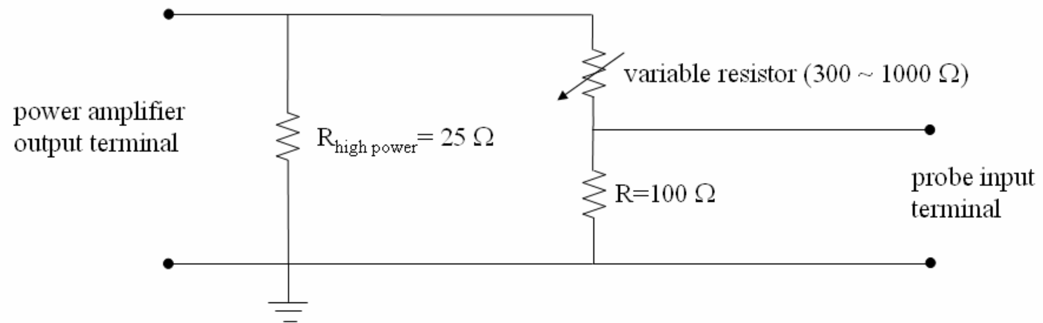

Figure A.8 Circuit diagram for RF power reduction.

VITA

Ryoung-han Kim received the B.S. and M.S. degrees in ceramic engineering from Yonsei University, Seoul, Korea, in 1997 and 2000, respectively.

From 1997 to 2000, he was with the Korea Institute of Science and Technology as a student research scientist and worked in the area of integrated optics. Since 2001, he has been a research assistant in the Department of Electrical Engineering, Texas A&M University, College Station where he received his Ph.D. degree in December 2005. His Research interest has been in the area of integrated optics. He is a member of the IEEE. He can be reached at the following address:

Ryoung-han Kim

Department of Electrical Engineering

Texas A&M University

College Station, TX 77843-3812

USA